

# An Optimized Multi-Dimensional Interpolation Scheme for Computational Aeroacoustics Applications Using Overset Grids\*

Christopher K.W. Tam<sup>†</sup>
Department of Mathematics, Florida State University, Tallahassee, Florida, 32306-4510, USA

and

Fang Q. Hu<sup>‡</sup>

Department of Mathematics & Statistics, Old Dominion University, Norfolk, Virginia, 23529, USA

A quantitative error analysis of multi-dimensional interpolation using regular or irregular stencils is carried out in wave number space. An optimized interpolation method is then developed. In this method, the interpolation coefficients are determined so as to minimize the interpolation error over a large band of wave numbers. This optimized multi-dimensional interpolation scheme is designed primarily for use in overset grid solutions of computational aeroacoustics problems. Comparisons of interpolation errors using the present method and the standard methods including the use of tensor products and Lagrange polynomials as interpolation basis functions are provided. An interpolation stencil, regular in a specific curvilinear coordinate system, is, invariably, irregular when another coordinate system is used as the frame of reference. For global interpolation, necessary for overset grid solutions, the errors incurred by using regular versus irregular stencils are not the same. This issue is investigated. The optimized multi-dimensional interpolation scheme is applied to the numerical solution of a number of acoustic scattering problems as well as a sliding interface problem via overset grid methodology. The computed results are in excellent agreements with exact solutions.

#### I. Introduction

Computational Aeroacoustics (CAA) and Computational Fluid Dynamics (CFD) methods are generally quite different. Standard CFD methods are largely low-order (first or second order). In most aeroacoustic problems, the sound fields are usually very small in amplitude relative to the mean flow. Typically, the ratio of amplitudes is of the order of  $10^{\square 4}$  or less<sup>1,2</sup>. To capture sound waves accurately, a high-resolution computation scheme is, therefore, required. Sound waves propagate at the speed of sound plus the local flow velocity. To ensure that the computed sound waves propagate at the correct speed, the computation scheme must have the correct group velocity over a broadband of wave numbers. To avoid excessive propagation errors in CAA, the computation scheme must also be nearly non-dispersive and non-dissipative<sup>1,2</sup>. This can be achieved only by the use of large stencil (high-order), high-resolution schemes.

Many aeroacoustics problems, e.g. fan noise<sup>3,4</sup> and airframe noise<sup>5</sup>, involve complex shapes and geometries. One of the most pressing need in CAA is the development of computation methods that can capture and support sound wave propagation and generation accurately and efficiently in the presence of complex solid surfaces. In CFD, problems with complex geometry are routinely treated using unstructured mesh or overset grid. Experience indicates that solutions on an unstructured mesh are best calculated by finite volume methods. However, finite volume methods are usually of first or second order. Thus, unless a high-order scheme on unstructured mesh becomes available, CFD methods on unstructured mesh are not suitable for aeroacoustic problems. For overset grid approach,

<sup>\*</sup> Copyright © 2004 by C.K.W. Tam and Fang Q. Hu. Published by the American Institute of Aeroacoustics and Astronautics, Inc. with permission.

<sup>†</sup> Robert O. Lawton Distinguished Professor, Department of Mathematics, Fellow AIAA.

<sup>‡</sup> Professor, Department of Mathematics & Statistics, Member AIAA.

structured meshes are often used to form the basic grids. It is, therefore, possible to use established and proven large stencil, high-resolution CAA methods for primary computation. To maintain high resolution over the entire computation domain, it is sufficient that the data transfer procedure between overlapping grids have similar accuracy and high resolution. The objective of this investigation is to develop a multi-dimensional optimized high-resolution interpolation scheme to facilitate the data transfer process.

One distinct advantage overset grid has over unstructured mesh is that body fitted grid may be used around solid surfaces. For viscous problems, a boundary layer will inevitably develop adjacent to solid surfaces. A natural and accurate way to resolve thin boundary layer flows computationally is to use body fitted grid. Hence, for aeroacoustic problems for which boundary layer flow and boundary layer noise are important, the use of a high resolution overset grid method is advantageous. In a variety of aeroacoustic problems, solid surfaces may move relative to each other. For instance, one dominant source of fan noise is the cutting of the wakes of the rotor blades by the stator. Figure 1 is a cascade (two dimensional) representation of a fan stage. The rotor blades rotate at high speed relative to the stator. For calculating the flow or sound transmission through the row of rotor blades, a natural choice is to use a computation domain fixed to the rotor. On the other hand, for the purpose of calculating the cutting of the wakes of the rotor blades by the stator blades, a natural choice is to use a computation domain fixed to the stator. Thus the two computation domains move relative to each other giving rise to a sliding interface problem. In this work, it will be shown that such sliding interface problem can be treated by overset grid concept. It is demonstrated later that sound waves as well as vorticity and entropy waves are transmitted accurately through such an interface using the optimized high-resolution multi-dimensional interpolation scheme.

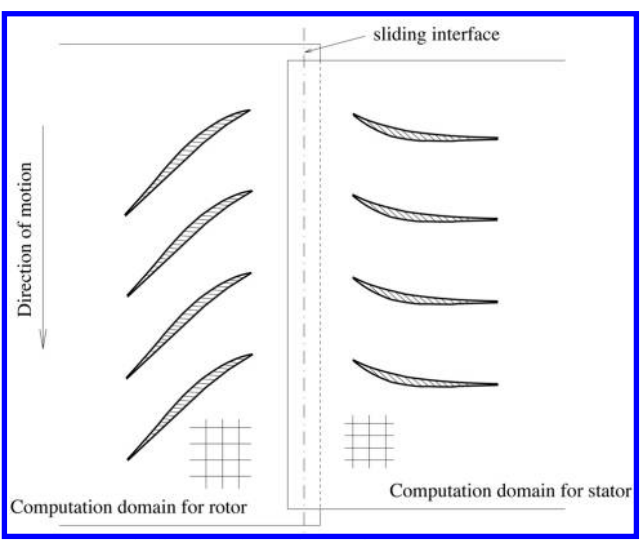


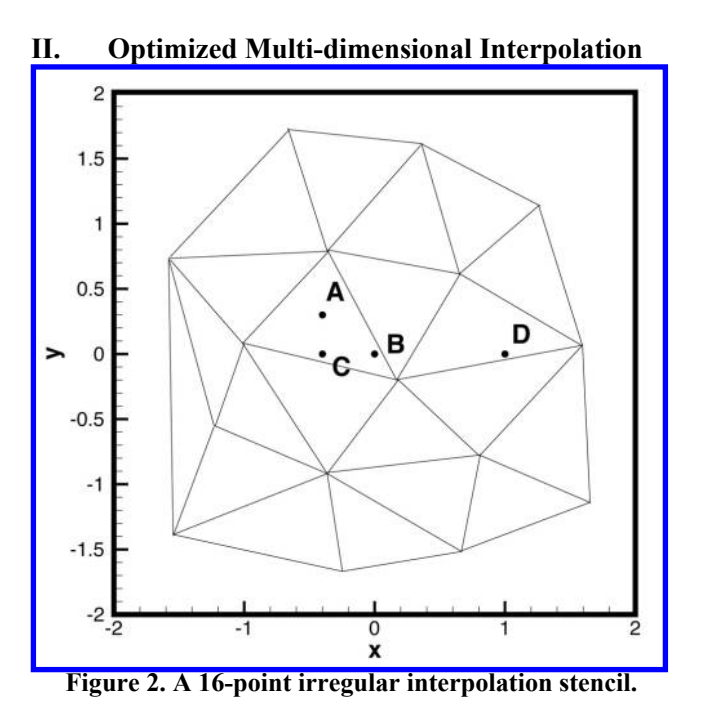
Figure 1. Sliding interface of a rotor and a stator.

Delfs<sup>6</sup>, Yin and Delfs<sup>7</sup> and Lee and Baeder<sup>8</sup> appear to be the first to use overset grid in CAA. Recently, the method has been improved by Scherer and Scott<sup>9</sup> as well as Scherer and Visbal<sup>10</sup>. They used compact scheme<sup>11</sup> as the basic method of computation. For data transfer between overlapping grids, they employed Lagrange polynomial interpolation. Another popular interpolation scheme is based on tensor product. Both the Lagrange polynomial interpolation as well as tensor product interpolation have been in use for a long time and are well documented in numerical analysis books. However, these methods as discussed in books appear to suffer a critical shortcoming in that there is no quantitative evaluation of the interpolation error. To be specific, there is a qualitative error estimate in terms of truncation order based on Taylor series expansion with respect to the mesh spacing. But there is no quantitative (absolute) error estimate. The problem is that, without a quantitative error evaluation, one does not know precisely which interpolation scheme is better and if better, how much better. Also one does not know how large an interpolation stencil is necessary to match the resolution of the computation scheme in an overset grid approach.

Recently, Tam and Kurbatskii<sup>12</sup> investigated why extrapolation could lead to numerical instability in a computation whereas interpolation does not have a similar problem. They formulated a wave number analysis to quantify both extrapolation and interpolation errors in one dimension. By means of wave number analysis, they developed an optimized interpolation and extrapolation method. Scherer and Scott<sup>13</sup> performed an error analysis comparing the optimized interpolation method of Tam and Kurbatskii and the B-Spline method. They showed that

the optimized scheme is far superior. In this work, the optimized interpolation method of Tam and Kurbatskii is extended to multi-dimensions. The interpolation error is quantified in multi-dimensional wave number space. In multi-dimensional interpolation, the interpolation stencil may be regular or irregular. The relative performance in using regular and irregular interpolation stencils for wave computation is discussed in a later section.

The rest of this paper is as follows. In Section 2, an optimized multi-dimensional interpolation method is developed. To improve the accuracy of the method over low wave numbers, additional constraints may be imposed. This is discussed in Section 3. Section 4 is a study of interpolation errors. Comparisons between the interpolation errors of the optimized scheme and that of the tensor product interpolation and Lagrange interpolation are reported. Global interpolation errors using regular and irregular interpolation stencils are then investigated. Applications of overset grid methodology using the optimized interpolation scheme to several wave scattering problems are described in Section 5. Favorable agreements between computed results and exact solutions are found. Solution of the fan noise sliding interface problem by means of the optimized interpolation method is also reported in Section 5. Finally, a summary of this work and concluding remarks are given in Section 6.



We will first develop the idea and methodology of optimized multi-dimensional interpolation. For simplicity, we will discuss two-dimensional interpolation in detail. The generalization to three dimensions is fairly straightforward. Consider an interpolation stencil in the computational domain as shown in Fig. 2. Without loss of generality, we will regard the computation domain as the  $x \sqcup y$  plane. However, x and y may be a set of curvilinear coordinates in the physical domain. For interpolation purposes, the values of a function f(x,y) are given at the stencil points  $(x_j,y_j)$ , j=1,2,...,N for an N-point stencil. The objective is to estimate the value  $f(x_0,y_0)$  at a general point P at  $(x_0,y_0)$ . By definition of interpolation (not extrapolation) the point P lies within the boundary of the stencil as defined by Fig. 2. Let  $d_j$  be the distance between neighboring points of the stencil. A useful length scale is

$$\Box = \frac{1}{K} \bigsqcup_{i=1}^{K} d_{i} \tag{1}$$

where K is the number of links between stencil points. The most general interpolation formula has the form

$$f(x_0, y_0) = \prod_{j=1}^{N} S_j f(x_j, y_j)$$
(2)

Different interpolation methods determine the coefficient  $S_i$  in different ways.

We will assume that the function f(x, y) to be interpolated has a Fourier inverse transform, such that

$$f(x,y) = \prod_{\square} f(\square,\square) e^{i(\square x + \square y)} d\square d\square$$
(3)

The direct Fourier transform is

$$\tilde{f}(\Box,\Box) = \frac{1}{(2\Box)^2} \prod_{\Box} f(x,y) e^{\Box i(\Box x + \Box y)} dx dy \tag{4}$$

where ([],[]) are the wave numbers in the x and y direction, respectively.

Let  $A([],[]) = |\tilde{f}([],[])|$  and  $[]([],[]) = \arg[\tilde{f}([],[])]$ . We may rewrite (3) as

$$f(x,y) = \prod_{\square} A(\square,\square) e^{i(\square x + \square y + \square(\square,\square))} d\square d\square$$
(5)

$$f_{\Pi\Pi} = e^{i\left[\left[Dx + \left[Dy + D(\Pi, \Pi)\right]\right]\right]} \tag{6}$$

Here all simple waves are assumed to have unit amplitude; i.e., A([], []) = 1.0. It is easy to find,

$$E_{\text{local}}^{2} = \left| e^{i(\Box x_{0} + \Box y_{0} + \Box)} \Box \Box_{j=1}^{N} S_{j} e^{i(\Box x_{0} + \Box y_{0} + \Box)} \right|^{2}$$

$$= \left| 1 \Box \Box_{j=1}^{N} S_{j} e^{i[\Box \Box ((x_{j} \Box x_{0}) / \Box) + \Box \Box ((y_{j} \Box y_{0}) / \Box))} \right|^{2}$$

$$(7)$$

$$E = \prod_{\square} \prod_{j=1}^{N} S_{j} e^{i[\square ((x_{j} \square x_{0})/\square) + \square ((y_{j} \square y_{0})/\square))} d(\square ) d(\square )$$
(8)

If the function to be interpolated is a constant, which corresponds to setting  $\Box = \Box = 0$  in (6), we require the local interpolation error be zero. By (7), this leads to

$$\prod_{j=1}^{N} s_j \prod 1 = 0 \tag{9}$$

We propose to choose the interpolation coefficients,  $S_j$  (j = 1, 2, ..., N), such that  $E^2$  is a minimum subjected to constraint (9). This can readily be done by using the method of Lagrange multiplier. Let

$$L = \coprod_{\square \square} \left| 1 \bigsqcup_{j=1}^{N} S_{j} e^{i \left[ \mathcal{D}((x_{j} \square x_{0}) / \square) + \mathcal{D}((y_{j} \square y_{0}) / \square) \right]} \right| d \square d \square + \square = \sum_{j=1}^{N} S_{j} \square 1$$

$$(10)$$

where  $\prod$  is the Lagrange multiplier. The conditions for L to be a minimum are

$$\frac{\partial L}{\partial S_i} = 0, \qquad \frac{\partial L}{\partial \Box} = 0, \qquad j = 1, 2, \dots, N$$
 (11)

It is easy to find the condition  $\partial L/\partial S_i = 0$  yields,

$$2\operatorname{Re}\left[\prod_{\square \square}^{\square} e^{\operatorname{Id}_{\mathbb{Q}((x_j\square \times 0)^{\prime}\square)+\mathcal{Q}((y_j\square \times 0)^{\prime}\square)}}\prod_{k=1}^{\square}\prod_{k=1}^{N} S_k e^{\operatorname{Id}_{\mathbb{Q}((x_k\square \times 0)^{\prime}\square)+\mathcal{Q}((y_k\square \times 0)^{\prime}\square)}}\prod_{l=1}^{\square} dl \right] dl + \square = 0$$

$$(12)$$

where Re{ } is the real part of { }. Similarly it is easy to find  $\partial L/\partial \Gamma$  leads to,

$$\prod_{j=1}^{N} S_j \prod 1 = 0 \tag{13}$$

which is constraint (9).

(12) and (13) form a linear matrix system of (N+1) unknowns for  $S_j$  (j=1,2,...,N) and  $\square$ . It turns out all the integrals of (12) can be evaluated in closed form. This allows the matrix elements to be written out explicitly. The values of  $S_j$  may be found by solving the matrix system,

$$\mathbf{AS} = \mathbf{b} \tag{14}$$

where vector  $\mathbf{S}^{\mathbf{T}} = (S_1 \ S_2 \ S_3 \ \cdots \ S_N \ \square)$ . Note: Superscript  $\mathbf{T}$  denotes the transpose. The elements of the coefficient matrix  $\mathbf{A}$  and vector  $\mathbf{b}$  are given by,

$$A_{jk} = \begin{bmatrix} \Box 4 \Box^{2}, & j = k \\ & \Box & 4 \Box^{2} & & \Box & (x_{k} \Box x_{j}) \Box & \Box & (y_{k} \Box y_{j}) \Box & j \neq k \end{bmatrix}$$

$$(15)$$

$$(j, k = 1, 2, \dots, N)$$

$$A_{j(N+1)} = \frac{1}{2}, \qquad j = 1, 2, ..., N$$
 (16)

$$A_{(N+1)_k} = 1, j = 1, 2, ..., N$$
 (17)

$$A_{(N+1)(N+1)} = 0 (18)$$

$$b_{(N+1)} = 1 (20)$$

Note: In the case  $x_j = x_k$  and/or  $y_j = y_k$  or  $x_j = x_0$  or  $y_j = y_0$  the limit forms of the above formulas are to be used. Computationally, the limit forms are used wherever  $|x_j| |x_k| < |y_j| |y_k| < |x_j| |x_k| < |x_j| |x_k|$ 

It is useful to point out that  $A_{jk}$  depends on  $\square$  and I/I as well as the coordinates of the stencil points only. The coordinates of the point to be interpolated to,  $(x_0, y_0)$ , appears only in  $b_j$ . Thus if many values of f are to be interpolated using the same stencil, A and  $A^{\square I}$  need only be computed once.

For error estimate purposes, the following symmetry properties of the local error, given by (7), can easily be derived.

$$E_{\text{local}}(\square,\square) = E_{\text{local}}(\square\square,\square\square) \tag{21}$$

$$E_{\text{local}}(\square \square, \square) = E_{\text{local}}(\square, \square \square)$$
(22)

Thus once  $S_j$ 's are found,  $E_{local}$  can be calculated by (7). Upon invoking (21) and (22), it is sufficient to examine  $E_{local}(\square,\square)$  over the upper half of the  $\square$   $\square$   $\square$  plane for  $\square$   $\square$   $\square$   $\square$   $\square$   $\square$   $\square$ .

#### **III.** Order Constraints

For small  $\prod$ , it is often desirable to require interpolation formula (2) to be accurate to a specified order of Taylor series expansion in  $\prod$ . This requirement imposes a set of constraints on the interpolation coefficients  $S_j$ . To find these constraints in their simplest form, we may expand  $f(x_j, y_j)$  about  $(x_0, y_0)$  to obtain,

$$f(x_j, y_j) = f(x_0, y_0) + \prod_{p,q} \frac{1}{p!q!} \frac{1}{\partial x^p \partial y^q} \prod_{\alpha_0, y_0} (x_j \square x_0)^p (y_j \square y_0)^q$$
(23)

On substituting (23) into (2), it is found

$$f(x_0, y_0) = f(x_0, y_0) + \begin{bmatrix} x_0 \\ y_0 \end{bmatrix} +$$

Thus, if we truncate (24) to order  $\square^M$ ,  $S_i$  must satisfy the following conditions.

$$\prod_{j=1}^{N} S_j = 1, \qquad M = 0$$
(25)

$$\prod_{j=1}^{N} (x_j \square x_0)^p (y_j \square y_0)^q S_j = 0, \qquad 1 \square p + q \square M$$
(26)

From (26) it is easy to see that if the order of truncation is increased from  $(M \square 1)$  to M, (M+1) more constraints are added. Therefore, the total number of constraints, T, to be satisfied, if (24) is truncated at  $M^{th}$  order, is

$$T = 1 + 2 + 3 + \dots + (M+1) = \frac{1}{2}(M+1)(M+2)$$
(27)

It is possible if  $(x_j, y_j)$ , j = 1, 2, ..., N are points on a highly regular grid, the total number of independent constraints given by (25) and (26) is less than that calculated by (27). Degeneracies would occur when a number of  $x_j$ 's or  $y_j$ 's are the same. In this case, only the linearly independent constraints need to be imposed.

Now for a given interpolation stencil with a given set of points  $(x_j, y_j)$ , j = 1, 2, ..., N, the interpolation coefficients  $S_j$  for the point  $(x_0, y_0)$  may be found by minimizing the total error  $E^2$ , given by (8), subjected to order constraints (25) and (26). This constrained minimization problem can again be easily solved by the method of Lagrange multipliers. Let

$$\mathcal{L} = \prod_{\square \square} \left| \prod_{j=1}^{N} S_{j} e^{i \left[ \square((x_{j} \square x_{0}) / \square) + \square((y_{j} \square y_{0}) / \square) \right]} \right|^{2} d \square d \square + \prod_{j=1}^{N} S_{j} \square 1 + \prod_{n,m} \square_{mn} \square_{j} S_{j} \left( x_{j} \square x_{0} \right)^{n} \left( y_{j} \square y_{0} \right)^{m} \square$$

$$(28)$$

where n, m = 0, 1, 2, ..., M;  $n + m \sqcap M$ ; n and m are not both equal to zero. M is the order of truncation. Since the total number of constraints (T as given by (27)) cannot exceed the number of stencil points, it is understood that T < N. The conditions for a minimum are:

$$\frac{\partial \mathcal{L}}{\partial S_{j}} = 0 \tag{29}$$

$$\frac{\partial \mathcal{L}}{\partial \Pi} = 0 \tag{30}$$

$$\frac{\partial \mathcal{L}}{\partial \square_{mn}} = 0 \tag{31}$$

Again, (29) to (31) lead to a linear matrix equation for the unknowns  $S_j$ ,  $\square$  and  $\square_{mn}$ . Let the transpose of the vector **X** and **d** be defined by,

$$\mathbf{X}^{\mathbf{T}} = \begin{pmatrix} S_1 & S_2 & \cdots & S_N & \square & \square_{10} & \square_{01} & \square_{20} & \square_{11} & \square_{02} & \cdots & \square_{mn} & \cdots & \square_{0M} \end{pmatrix}$$
(32)

$$\mathbf{d}^{\mathbf{T}} = (b_1 \ b_2 \ \cdots \ b_N \ 1 \ 0 \ 0 \ \cdots \ \cdots \ 0 \ 0)$$
 (33)

where  $b_j$ 's are given by (19) and (20). It is easy to establish by means of (29) to (31) that **X** is the solution of the matrix equation

$$\mathbf{BX} = \mathbf{d} \tag{34}$$

The coefficient matrix **B** may be partitioned into four submatrices as,

$$\mathbf{B} = \begin{bmatrix} \mathbf{A} & \mathbf{C} \\ \mathbf{C}^{\mathrm{T}} & \mathbf{0} \end{bmatrix} \tag{35}$$

**A** is a (N+1) by (N+1) square matrix. It is the same as that of (14). **C** is a (N+1) by  $(T \square 1)$  matrix.  $C^T$  is the transpose of **C**. The zero matrix **0** is a square matrix of size  $(T \square 1)$ . On writing out in full the elements of matrix **C** are,

Again once (34) is solved, the interpolation coefficients  $S_j$ 's are found. By substituting the values of  $S_j$ 's into (7), the local interpolation error,  $E_{local}$ , at wave number ( $\square$ ,  $\square$ ) may be computed.

# IV. Interpolation Errors in Wave Number Space

We will now test the accuracy of the proposed optimized multi-dimensional interpolation scheme. This is done in several ways including comparisons with standard interpolation methods. Before doing so, we wish to point out that in using this method as a part of an overset grid large scale computation, the interpolation stencil may be regular or irregular depending on the basic computation stencils used. Figure 2 shows a 16-point irregular interpolation stencil. For reference purposes, the coordinates of the interpolation points of this stencil are given in Appendix B. Figure 3 shows a 16-point regular stencil in the form of a square. At this point, we would like to report that as a part of the present investigation, we have carried out interpolation error analysis for the four points A, B, C, D shown in both Figs. 2 and 3. Our finding is that the errors for points A, B and C are very similar. For this reason, in this paper, we will only present and discuss the interpolation errors of A and D. We would like to consider point A as typical of all the points located around the center of the stencil. Also we would like to regard point D as typical of all the points located close to the boundary of the stencil.

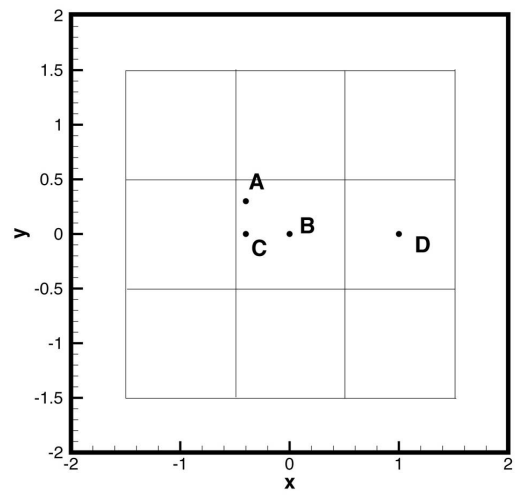


Figure 3. A 16-point regular stencil in the form of a square.

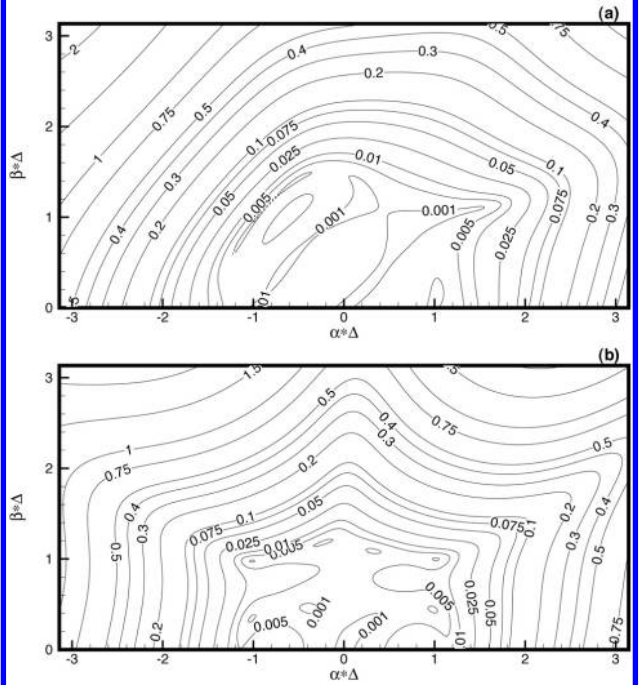


Figure 4. Contours of local interpolation error,  $E_{local}$ , in the  $\square$  plane for the irregular stencil of Fig. 2 using the optimized interpolation scheme. (a) at A, (b) at D.

Earlier, Tam and Kurbatskii [12] investigated extrapolation and interpolation in one dimension. They pointed out that extrapolation could lead to very large error in the high wave number components. For grid-to-grid oscillations with wave number  $\prod = \prod$ , some extrapolation schemes could incur a relative error as large as several hundreds. This large error is the mechanism for large numerical amplification that often leads to numerical instability. To ensure that the present proposed multi-dimensional interpolation would not lead to numerical instability associated with large errors at high wave numbers, we have examined the local error in the wave number space [] [] [] for every case reported here. Our finding is that there is no large error amplification at high wave number for interpolation using the proposed scheme. Figure 4 shows the local error,  $E_{local}$ , contours in the  $\square$ plane. In calculating  $E_{local}$ , // has been set equal to 1.2. We have found through numerical experimentation that  $\Pi = 1.2$  is a reasonably good value to use. This value is used throughout the present investigation. As can readily be seen in Fig. 4 there is no large error even for high wave numbers. In most aeroacoustics applications, the range of wave number that is of interest is [1.0] [1.0] [1.0]. In order to show error maps with more clarity, we will only show the low wave number portion of the mild plane. We would like to assure that the local interpolation error for high wave numbers are similar to those of Fig. 4. It is also worthwhile to note that in the absence of significant amplification of high wave numbers, no extra artificial selective damping [14] or numerical filtering [11] would be needed when using the proposed interpolation scheme in a large scale computation.

#### 1) Effect of Order Constraints

The imposition of order constraints has definitely a significant impact on the local error distribution in the wave number space. It is beneficial in reducing the error in the low wave number region.

Figure 7 shows contours of local interpolation error,  $E_{local}$ , at A using the 16-point regular stencil of Fig. 3. Figures 7a, 7b and 7c are subjected to  $2^{nd}$ ,  $3^{rd}$  and  $4^{th}$  order constraints, respectively. Because of regularity of the stencil points,  $x_j = x_k$  and  $y_j = y_k$  occur repeatedly. There are only four independent values of  $x_j$  and  $y_j$  (j = 1, 2, ..., 16). This immediately leads to degeneracies in the  $4^{th}$  order constraints. To show this is, indeed, the case, recall that the interpolation coefficients are to be found by solving equation (34)  $\mathbf{BX} = \mathbf{d}$ . Here N is 16. Including the last row of submatrix  $\mathbf{A}$ , the last 15 rows of matrix  $\mathbf{B}$  are as follows,

If there is no degeneracy, the above fifteen row vectors must be linearly independent. We will now show that this is not the case.

Consider the following five of the fifteen row vectors

Since there are only four independent  $x_j$ 's, there are only four independent column vectors. It follows that there are only four independent row vectors as well. Similarly, there is also one degeneracy due to the fact that there are only four independent values of y coordinates. To impose  $4^{th}$  order constraint on the interpolation scheme, only 13 linearly independent conditions are imposed. Figure 7c is computed with only 13 constraints.

On comparing Figs. 7a, 7b and 7c, it is clear that the case with  $4^{th}$  order constraints turns out to have slightly more error than those with lower order constraints. On the other hand, the cases with  $2^{nd}$  order and  $3^{rd}$  order constraints are about the same. Figures 8a, 8b and 8c show similar error contours for the point D of Fig. 3. Again because of degeneracies with the  $4^{th}$  order constraints only 13 conditions are used in the optimization procedure. An inspection of these figures suggests that there are only minor differences among them. If minor differences in the distribution of interpolation error is acceptable, then the use of the  $2^{nd}$  order constraints would suffice when a highly regular stencil is used.

#### 2) Comparisons with Other Methods of Interpolation

Currently, interpolation is widely used in large scale computing. The most popular method is the polynomial interpolation method. If an irregular stencil with \$N\$ points is used, the interpolation formula is,

$$f(x,y) = \prod_{i=1}^{N} a_i \square_i (x,y)$$
(37)

where  $\Box(x,y)$ , j=1,2,...,N are polynomial basis functions. The values of f at the stencil points  $(x_i,y_i)$  are given. Let us denote

$$f_i = f(x_i, y_i) \tag{38}$$

The requirements that (37) satisfies (38) lead to a linear system for the coefficients  $a_i$ ; i.e.

$$\mathbf{Ma} = \mathbf{b} \tag{39}$$

where  $M_{ij}$  (the elements of  $\mathbf{M}$ ) =  $\prod_{i} (x_i, y_i)$ ;  $a_i$  (the elements of  $\mathbf{a}$ ) and  $b_i$  (the  $i^{th}$  element of  $\mathbf{b}$ ) =  $f_i$ .

Suppose the inverse of matrix **M** is  $\mathbf{M}^{\square 1}$ . We will denote the elements of  $\mathbf{M}^{\square 1}$  as  $e_{ij}$ . On premultiplying (39) by  $\mathbf{M}^{\square 1}$ , we obtain,

$$a_i = \prod_{k=1}^{N} e_{ik} f_k \tag{40}$$

On substituting (40) into (37), it is found

$$f(x,y) = \prod_{i=1}^{N} \prod_{k=1}^{N} e_{jk} f_k \prod_{i=1}^{n} \prod_{j=1}^{N} (x,y) = \prod_{k=1}^{N} \prod_{i=1}^{N} e_{jk} \prod_{j} (x,y) \prod_{j=1}^{n} f_k$$

$$\tag{41}$$

(41) is commonly rewritten in the form (see (2))

$$f(x_0, y_0) = \prod_{k=1}^{N} S_k f_k$$
 (42)

where

$$S_k = \prod_{j=1}^N e_{jk} \prod_j (x_0, y_0)$$

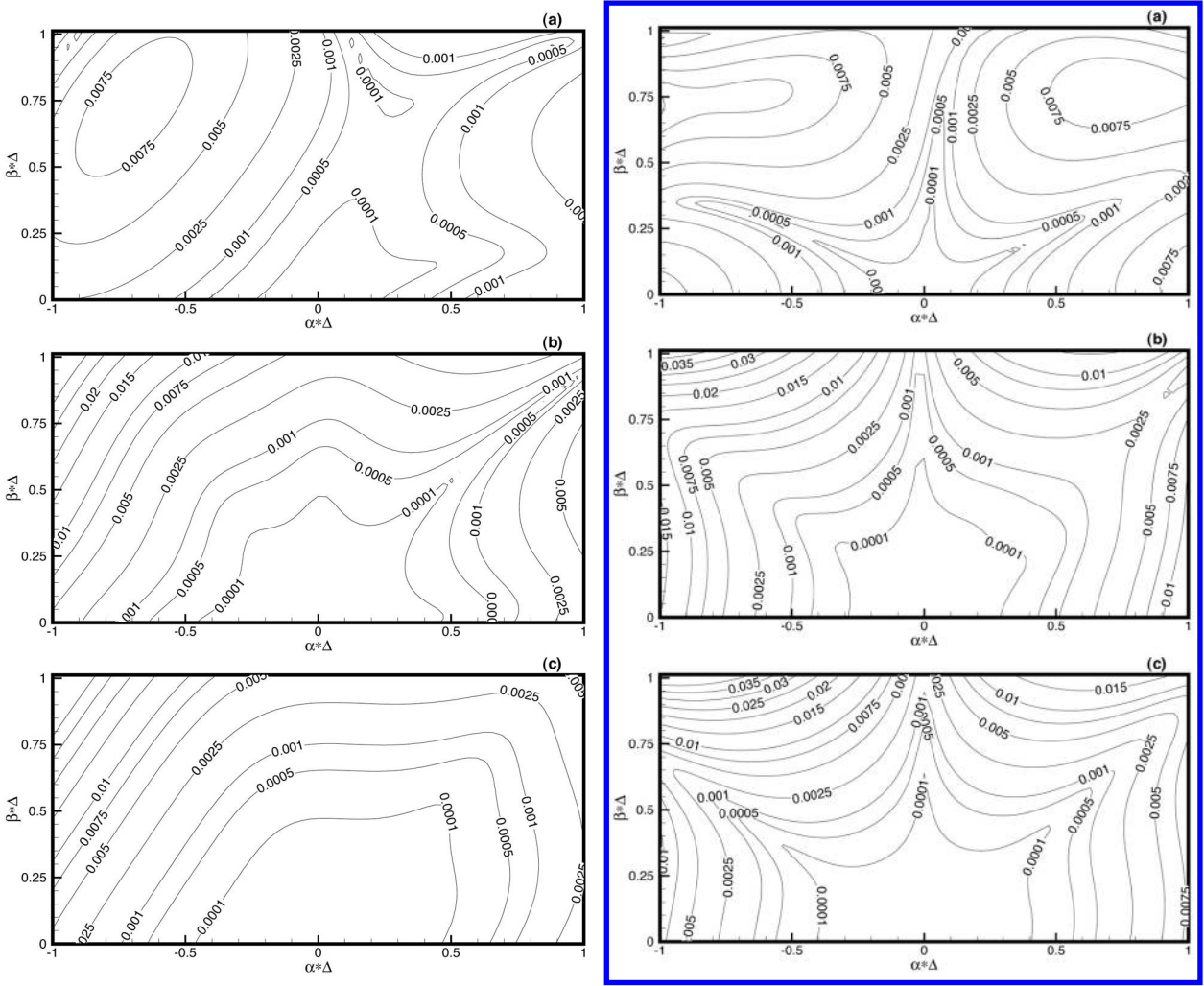


Figure 5. Contour maps of interpolation error,  $E_{local}$ , Figure 6. Contour maps of interpolation error,  $E_{local}$ , at A using the irregular stencil with order at D using the irregular stencil with order constraints. (a) Second order. (b) Third order. (c) constraints. (a) Second order. (b) Third order. (c) Fourth order.

Fourth order.

One usual choice for basis functions is tensor product basis functions in x and y. For example, for N = 16

$$\Box_{j}(x,y) = (1,x,x^{2},x^{3}) \quad (1,y,y^{2},y^{3})$$

Thus the tensor product basis functions are,

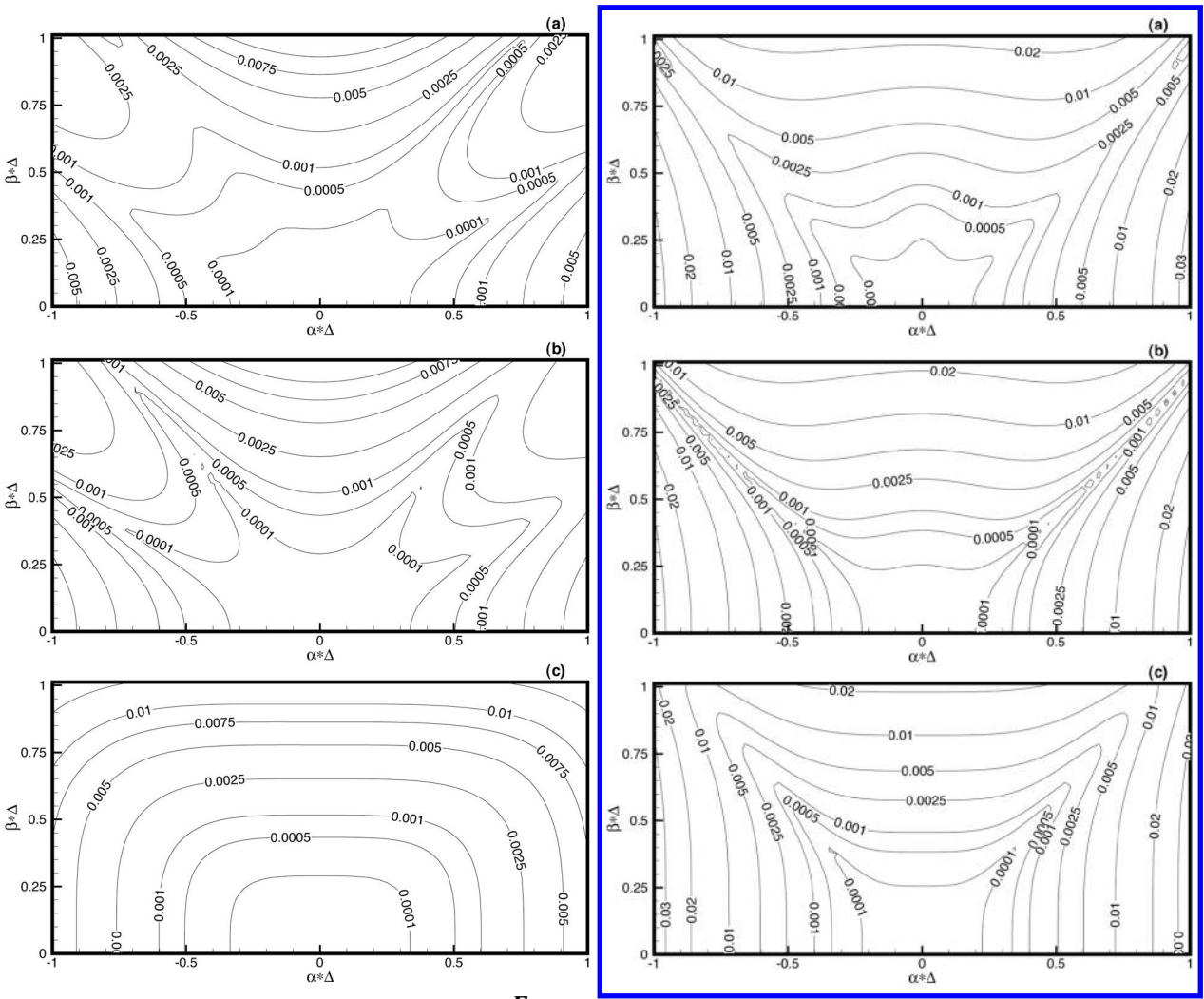


Figure 7. Contour maps of interpolation error,  $E_{\text{local}}$ , at A using the regular stencil with order constraints. (a) Second order. (b) Third order. (c) Fourth order.

Figure 8. Contour maps of interpolation error,  $E_{local}$ , at D using the regular stencil with order constraints. (a) Second order. (b) Third order. (c) Fourth order.

Another way to form basis functions is to choose a complete set of polynomials up to a certain order. For instance, there are 15 basis functions for polynomials up to order 4. The order set basis functions are

$$\square_{j}(x,y) = 1, x, y, x^{2}, xy, y^{2}, x^{3}, x^{2}y, xy^{2}, y^{3}, x^{4}, x^{3}y, x^{2}y^{2}, xy^{3}, y^{4}$$

One more basis function is to be added to form a basis of 16 functions. A simple choice could be  $x^3y^2$ .

Figures 9a, 9b and 9c show the error contour maps for the point A of the irregular stencil of Fig. 2 using the  $4^{th}$  order constrained optimization method, the tensor product basis and the order set basis polynomial interpolation. It is evident on comparisons that the use of tensor product basis interpolation would lead to high error. The optimized scheme is somewhat better than the order set basis method. Figures 10a, 10b and 10c show similar error contour maps for the point D. Again the tensor product basis interpolation has the largest error. The optimized method using  $4^{th}$  order constraints is just slightly better than the order set basis interpolation.

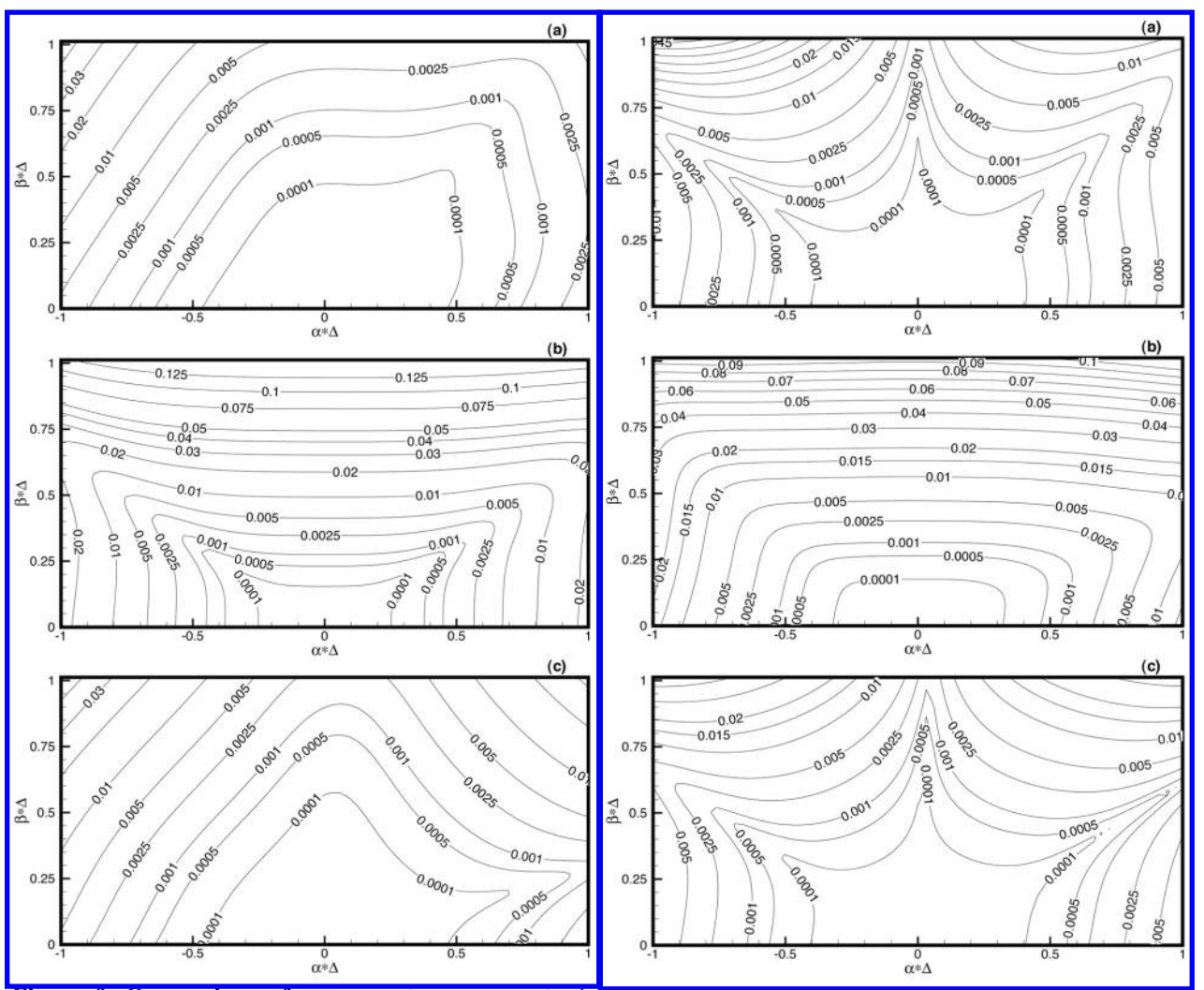


Figure 9. Comparison of error contour maps at A Figure 10. Comparison of error contour maps at Dmethod. (b) Tensor product basis. (c) Order set basis.

using the irregular stencil. (a) Fourth order optimized using the irregular stencil. (a) Fourth order optimized method. (b) Tensor product basis. (c) Order set basis.

When a regular stencil is used; e.g., that of Fig. 3, it is a common practice to use products of Lagrange polynomials for interpolation. For interpolating the value of a function f at a point  $(x_0, y_0)$ , the following formula is used.

$$f(x_0, y_0) = \prod_{i=0}^{3} \prod_{j=0}^{3} a_{ij} f(x_i, y_j)$$
(43)

where (for the stencil of Fig. 3)  $x_i = \begin{bmatrix} 1.5 + i & (i = 0,1,2,3) \\ i & (j = 0,1,2,3) \end{bmatrix}$  is the value of f(x, y) on the grid point  $(x_i, y_i)$  and  $a_{ii}$  is given by

$$a_{ij} = \prod_{\substack{\ell=0\\\ell \neq i}}^{3} \frac{\left(x_0 \square x_\ell\right)}{\left(x_i \square x_\ell\right)} \prod_{\substack{k=0\\k \neq j}}^{3} \frac{\left(y_0 \square y_k\right)}{\left(y_j \square y_k\right)}$$

$$\tag{44}$$

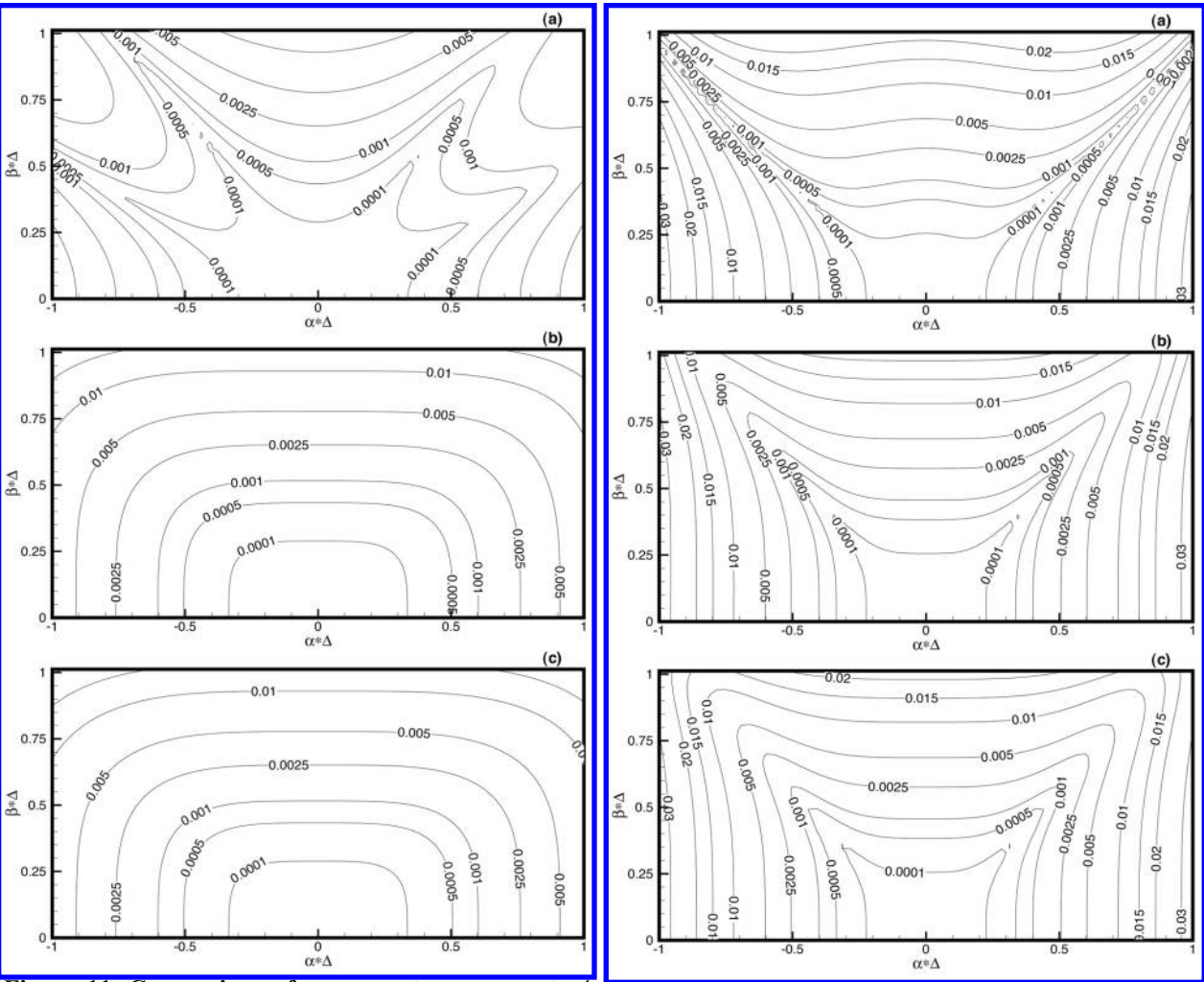
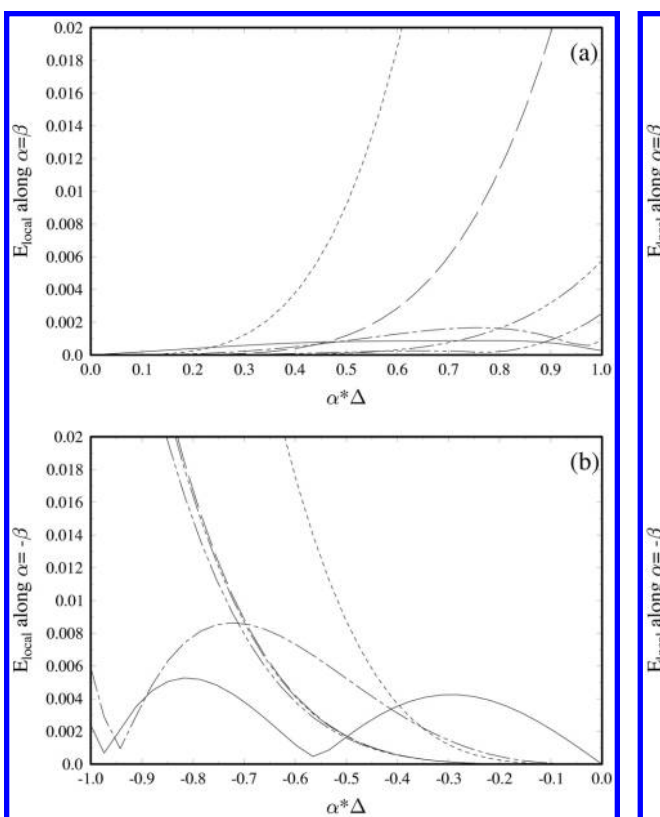


Figure 11. Comparison of error contour maps at Ausing the regular stencil. (a) Third order optimized using the regular stencil. (a) Third order optimized method. (b) Fourth order optimized method. (c) method. (b) Fourth order optimized method. (c) Lagrange interpolation.

Figure 12. Comparison of error contour maps at D Lagrange interpolation.

Figure 11 shows error contour maps for interpolation to point A using the regular stencil of Fig. 3. By comparison, it is easy to see that the 4<sup>th</sup> order constrained optimization method and the Lagrange interpolation method (Figs. 11b and 11c) have nearly identical local error. The error map configuration is very different from that of the 3<sup>rd</sup> order constraint (Fig. 11a). A closer examination reveals that the 3<sup>rd</sup> order constrained optimization method is the one with least error in the \frac{1}{11} \frac{1}{17} plane shown. Figure 12 provides similar comparisons for interpolation to the point D. Again the 4<sup>th</sup> order constrained optimization method and the Lagrange polynomial interpolation have nearly identical error contours. However, in this case, they are also nearly the same as that of the 3<sup>rd</sup> order constrained optimization method.

Finally, Figs. 13 and 14 provide comparisons of interpolation errors using different methods from a slightly different perspective. In these figures the local errors along the lines  $\Pi = \Pi$  and  $\Pi = \Pi$  of the  $\Pi$  plane of six methods are plotted. Figure 13 is for point A of the irregular stencil of Fig. 2. Figure 14 is for point D. It is easy to see that the Lagrange interpolation method and the high order constrained optimization method have low level of error for low wave numbers. However, the error increases rapidly as wave number increases. The low order constrained optimization scheme have higher level of error at low wave number. But the error remains low even when  $\prod$  and  $\prod$  are as large as 1.0. Thus for large scale computation where the resolved wave number range is [1] 0.9 (7 mesh points per wave length) the use of low or zero order constrained optimized interpolation method would be the best choice.



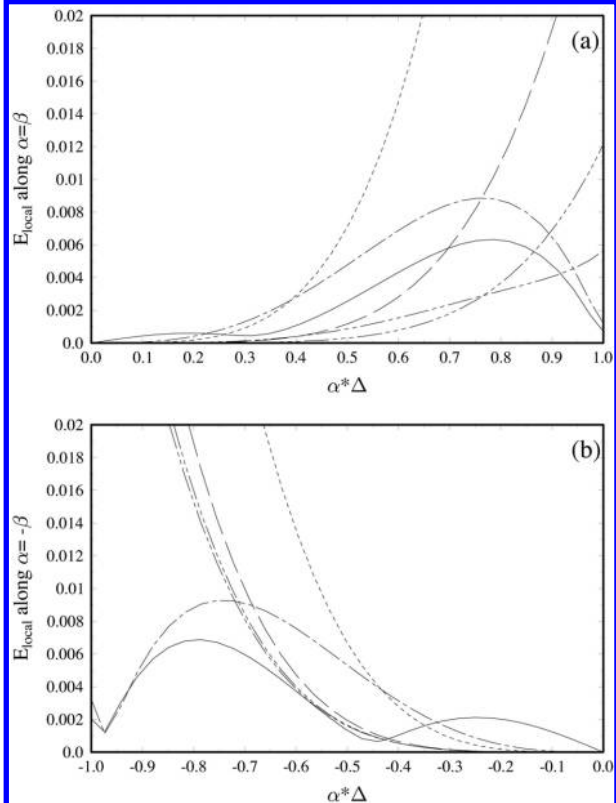


Figure 13. Comparison of local interpolation error, Figure 14. Same as Fig. 13 but for interpolation to  $E_{local}$ , at A along the lines (a)  $\square = \square$ , (b)  $\square = \square \square$  of the  $\prod \prod \prod$  plane using the irregular stencil and six interpolation methods. - - optimized method no order constraint; — • — • — 2<sup>nd</sup> order; — • • — • • 3<sup>rd</sup> order; — • • • — • • — 4<sup>th</sup> order; order set basis; ---- tensor product basis.

point D.

#### 3) **Global Interpolation**

An interpolation stencil may be in the form of a regular stencil in a curvilinear coordinate system but would be an irregular stencil when a different coordinate system is used as the frame of reference. For example, Fig. 15 shows a regular 16-point interpolation stencil of the polar coordinate system. That is if the  $r \square \square$  plane is used for computation, the interpolation stencil points form a regular stencil. But if the computation is done in Cartesian coordinates, namely the coordinates of the stencil points are specified in a Cartesian coordinate system, the interpolation points form an irregular stencil.

In overset grid computation and in other applications, extensive interpolation from one set of mesh points of one curvilinear coordinate system to the mesh points of another coordinate system becomes necessary. Global interpolation of this type may be carried out using either set of coordinate system. As a test case, consider a plane wave with wave vector **k** inclined at 30° to the x-axis in the x | y plane. The wave function  $\prod$  may be written as

$$\Box(x,y) = \operatorname{Re}\left\{e^{ik[x\cos(\Box/6) + y\sin(\Box/6)]}\right\} \tag{45}$$

where Re $\{ \}$  is the real part of  $\{ \}$ . The wave function can also be written in polar coordinates  $(r, \square)$  by a straightforward coordinate transformation, thus

$$\Box (r,\Box) = \operatorname{Re} \left\{ e^{ikr\cos(\Box\Box\Box/6)} \right\} \tag{46}$$

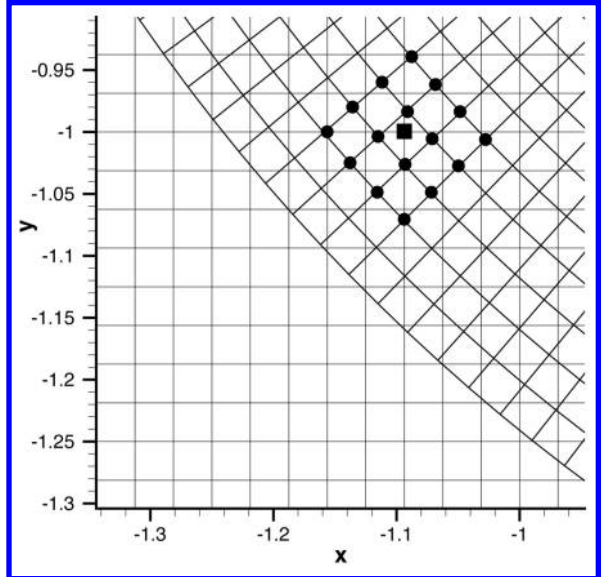


Figure 15. Interpolation from a polar grid to a Cartesian grid using a 16-point stencil.  $\Box x = \Box y = \Box r = 1/32$ ,  $\Box \Box = \Box /150$ .

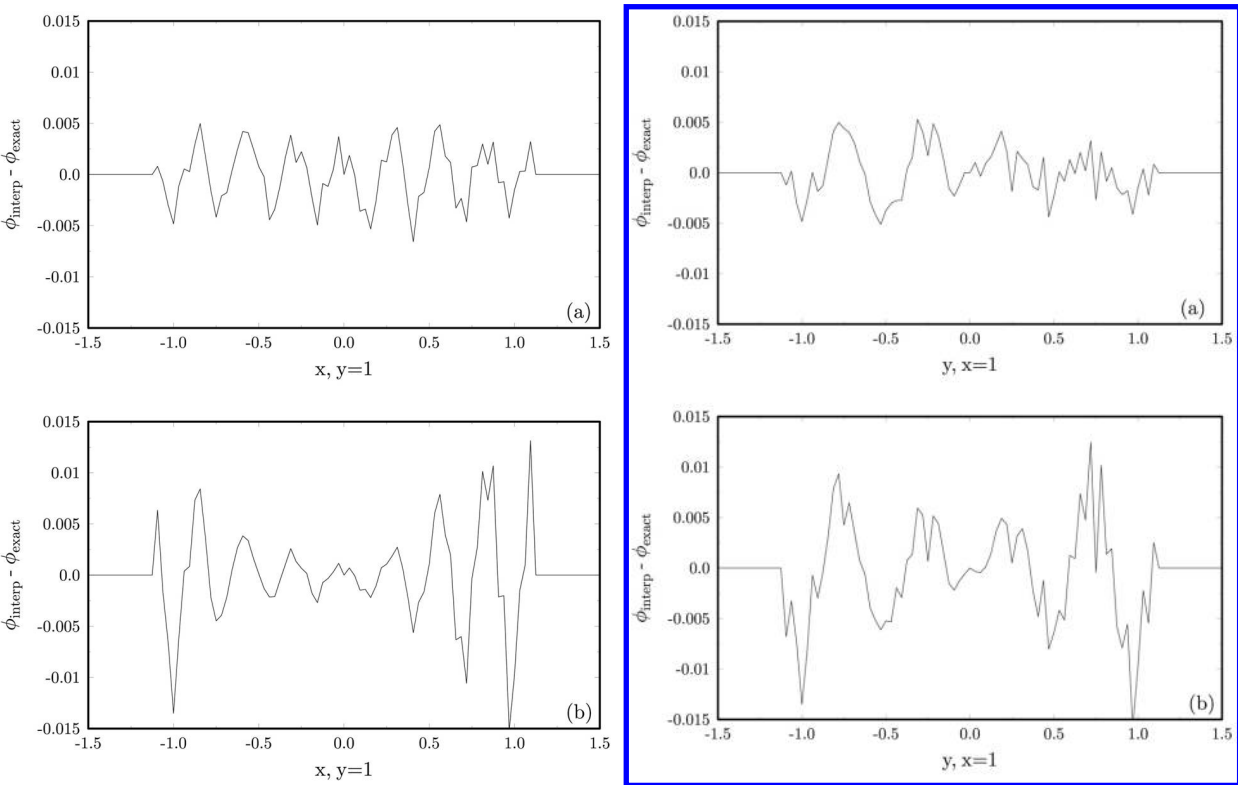


Figure 16. Distribution of interpolation error along the line y = 1. (a) Using a 16-point regular stencil in the  $r \sqcap \square$  plane. (b) Using a 16-point irregular stencil in the  $x \sqcup y$  plane.

Figure 17. Distribution of interpolation error along the line x = 1. (a) Using a 16-point regular stencil in the  $r \sqcap \sqcap$  plane. (b) Using a 16-point irregular stencil in the  $x \sqcup y$  plane.

Now let us use a mesh of  $\Box x = \Box y = 1/32$  in the Cartesian coordinates and  $\Box r = 1/32$ ,  $\Box \Box r = 1/150$  in the polar coordinate as shown in Fig. 15. We will let the values of  $\Box$  be known on the polar mesh points. Suppose we want to find  $\Box$  at the mesh points of the Cartesian coordinates by using a 16-point interpolation stencil. That is we want to

interpolate the values of  $\sqcap$  from the polar grid to the Cartesian grid. One obvious way is to refer the coordinates of all points to the polar coordinates system and perform the interpolation in the  $(r, \square)$  plane. In the  $(r, \square)$  plane the 16-interpolation points form a regular stencil. If the optimized interpolation scheme is used, it is easy to show that the matrix  $\mathbf{A}$  (for interpolation in polar coordinates, see (14)) is the same for all interpolation stencils. For this reason, the inverse coefficient matrix  $\mathbf{A}^{\square 1}$  needs to be computed only once. On the other hand, if the interpolations are carried out in the Cartesian coordinate system, the stencils are irregular. It follows that the matrix  $\mathbf{A}$  for each point to be interpolated to is different.

One piece of information one would like to know about global interpolation as described above is which way of interpolation, using regular or irregular stencils, would yield the least global error. For the example under consideration, the exact wave function on the Cartesian mesh is given by (45). We may perform the interpolation from polar mesh to the Cartesian mesh in both ways and compare the results with the exact wave function to assess the error. Figure 16a shows the interpolation error for the plane wave along the line y = 1.0 using the polar coordinates as the reference coordinates (regular stencils). Figure 16b shows the corresponding interpolation error when the interpolation is performed in the Cartesian coordinates (irregular stencil). It is evident from these figures that the error in Fig. 16b is more than twice as large as that in Fig 16a. This strongly suggests that when global interpolation is needed, it would be best if regular stencils are used. Figures 17a and 17b provide similar comparison of global interpolation error arising from the use of regular and irregular stencils along the line x = 1.0. Again the use of irregular stencils results in considerably larger interpolation error.

### V. Overset Grid Applications

#### A. Acoustic Wave Scattering by a Rigid Cylinder

We will consider acoustic wave scattering by a rigid cylinder. Near the cylinder the coordinate system of choice is the cylindrical polar coordinates centered at the axis of the cylinder. This coordinate system provides a body fitted grid around the cylinder. One significant advantage of using body fitted grid is the relative ease in enforcing the no through flow solid wall boundary condition using the highly accurate ghost point method of Tam and Dong [15]. Away from the cylinder, acoustic waves propagate with no preferred direction. The natural coordinate system to use is the Cartesian coordinates. Thus we will use a polar mesh around the cylinder and a Cartesian mesh away from the cylinder with an overlapping mesh region for data transfer.

Figure 18 shows the Cartesian mesh with a square hole around the cylinder. We will use the diameter, D, of the cylinder as length scale, speed of sound  $a_0$  as the velocity scale,  $D/a_0$  as the time scale,  $\Box_0$  (the density of the undisturbed gas) as the density scale, and  $\Box_0 a_0^2$  as the pressure scale. The mesh size is  $\Box x = \Box y = 1/32$ . Figure 19 shows the polar mesh with  $\Box r = 1/32$  and  $\Box \Box = \Box/150$ . The polar mesh extends to a distance of r = 1.5. The mesh overlap region is between the square and the outside edge of the polar mesh as shown in Fig. 19. Figure 20 is an enlarged view of the mesh overlap region. In the computation, the 7-point stencil DRP scheme [16] is used. Since the 7-point stencil DRP scheme is a central difference scheme, the values of the computation variables of the three rows and columns of the Cartesian mesh around the square hole are not computed by the time marching scheme. They are found by interpolation from the values of the polar mesh using a 16-point regular stencil. A typical stencil is shown in Fig. 15. For the polar mesh, the values of the Cartesian mesh using a 16-point regular stencil as shown in Fig. 21.

The governing equations are the full Euler equations. In dimensionless form, they are

#### Cartesian coordinates

$$\frac{\partial \Box}{\partial t} + u \frac{\partial \Box}{\partial x} + v \frac{\partial \Box}{\partial y} + \Box \frac{\partial u}{\partial x} + \frac{\partial v}{\partial y} = 0$$

$$\frac{\partial u}{\partial t} + u \frac{\partial u}{\partial x} + v \frac{\partial u}{\partial y} + \frac{1}{\Box} \frac{\partial p}{\partial x} = 0$$

$$\frac{\partial v}{\partial t} + u \frac{\partial v}{\partial x} + v \frac{\partial v}{\partial y} + \frac{1}{\Box} \frac{\partial p}{\partial x} = 0$$

$$\frac{\partial p}{\partial t} + u \frac{\partial p}{\partial x} + v \frac{\partial p}{\partial y} + \Box \frac{\partial u}{\partial x} + \frac{\partial v}{\partial y} = 0$$

$$(47)$$

Polar coordinates

$$\frac{\partial \square}{\partial t} + \frac{1}{r} \frac{\partial}{\partial r} \left( \square v_{r} r \right) + \frac{1}{r} \frac{\partial \square v_{\square}}{\partial \square} = 0$$

$$\frac{\partial v_{r}}{\partial t} + v_{r} \frac{\partial v_{r}}{\partial r} + \frac{v_{\square}}{r} \frac{\partial v_{r}}{\partial \square} \square \frac{v_{\square}^{2}}{r} + \frac{1}{\square} \frac{\partial p}{\partial r} = 0$$

$$\frac{\partial v_{\square}}{\partial t} + v_{r} \frac{\partial v_{\square}}{\partial r} + \frac{v_{\square}}{r} \frac{\partial v_{\square}}{\partial \square} + \frac{v_{r} v_{\square}}{r} + \frac{1}{\square} \frac{\partial p}{\partial \square} = 0$$

$$\frac{\partial p}{\partial t} + v_{r} \frac{\partial p}{\partial r} + \frac{v_{\square}}{r} \frac{\partial p}{\partial \square} + \square \frac{1}{r} \frac{\partial v_{r} r}{\partial \square} + \frac{1}{r} \frac{\partial v_{\square}}{\partial \square} = 0$$

$$\frac{\partial p}{\partial t} + v_{r} \frac{\partial p}{\partial r} + \frac{v_{\square}}{r} \frac{\partial p}{\partial \square} + \square \frac{1}{r} \frac{\partial v_{r} r}{\partial \square} + \frac{1}{r} \frac{\partial v_{\square}}{\partial \square} = 0$$
(48)

The solution of (47) is computed on the Cartesian mesh. The solution of (48) is computed on the polar mesh. (u,v) and  $(v_r,v_{\square})$  are related by,

$$u = v_r \cos \square \square v_{\square} \sin \square$$

$$v = v_r \sin \square + v_{\square} \cos \square$$

$$v_r = u \cos \square + v \sin \square$$

$$v_{\square} = \square u \sin \square + v \cos \square$$

In solving the Euler equations by the DRP scheme, artificial selective damping terms [14,1] are added to the discretized equations. These terms are used to remove spurious short waves that are generated at surfaces of discontinuity such as the solid cylinder surface of the present problem.

#### 1. Transient Scattering Problem

We consider the scattering of an initial pressure pulse by the cylinder. For this problem, the Euler equations are solved with the initial conditions, t = 0

$$u = v = 0, p = \frac{1}{\Box} + \Box \exp\left[\left(\ln 2\right) \frac{\left(x \Box 4\right)^2 + y^2}{0.2^2}\right] \Box = \Box \Box \Box \Box \Box + p (49)$$

With a very small initial pulse amplitude ( $\square = 10^{\square 4}$ ), the computed solution is identical to the solution of the linearized Euler equations. The cylinder scattering problem governed by the linearized Euler equation is a benchmark problem of the  $2^{nd}$  CAA Workshop on Benchmark Problems [17]. An exact solution has been found. The exact solution is given in Appendix C at the end of this paper.

Figure 22 shows the computed pressure contours at t = 1.6, 4.0 and 6.4. The computed contours and the contours of the exact solution are indistinguishable (the difference is less than the thickness of the contour lines). The direct acoustic pulse and the scattered pulse can clearly be seen in this figure. For a more comprehensive comparison between the numerical and exact solution, the pressure time-history at three locations with Cartesian coordinates (-5,0), (-4,4) and (0,5) are plotted in Fig. 23. Plotted in these figures also are the exact solution. The differences between the exact (dashed line) and computed solution are again very small.

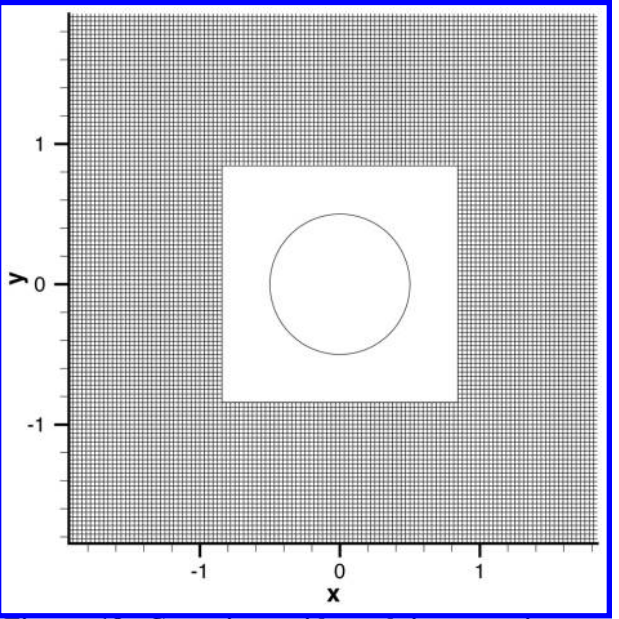


Figure 18. Cartesian grid used in acoustic wave scattering by a cylinder problem.

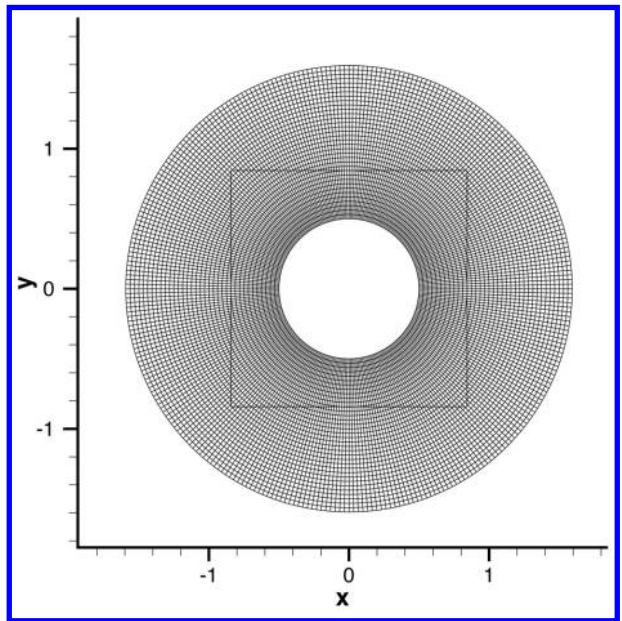


Figure 19. Polar grid used in acoustic wave scattering problem. Square indicates the inner boundary of the Cartesian grid.

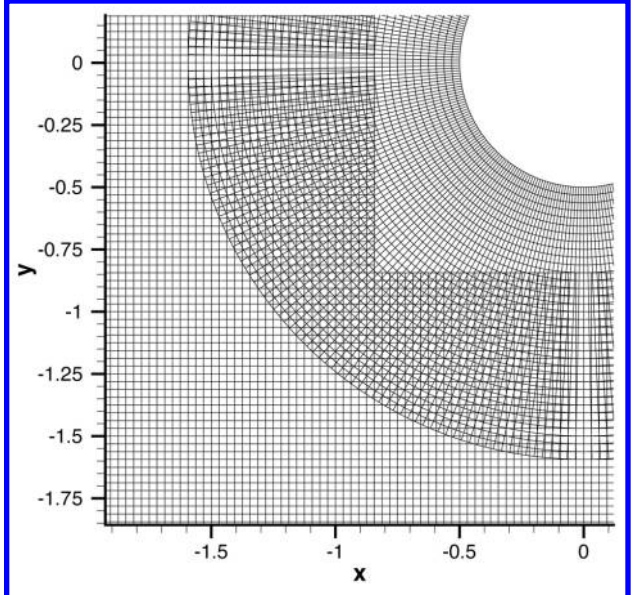


Figure 20. The overlapping region of the Cartesian and polar grids.

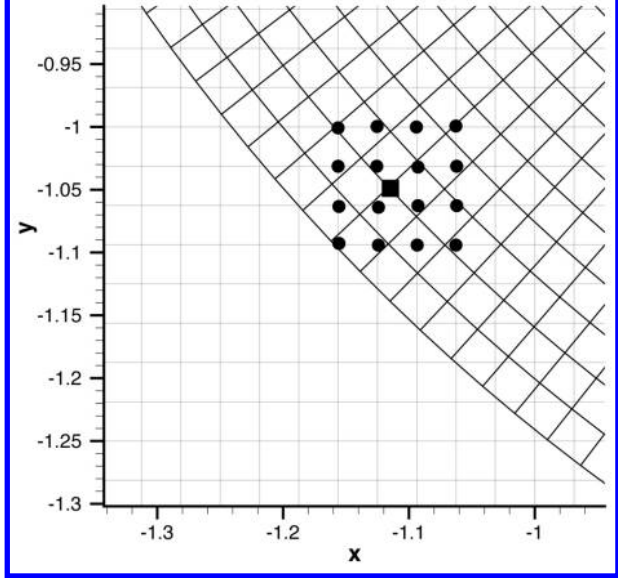


Figure 21. 16-point stencil used to interpolate computation variables from the Cartesian grid to the polar grid.

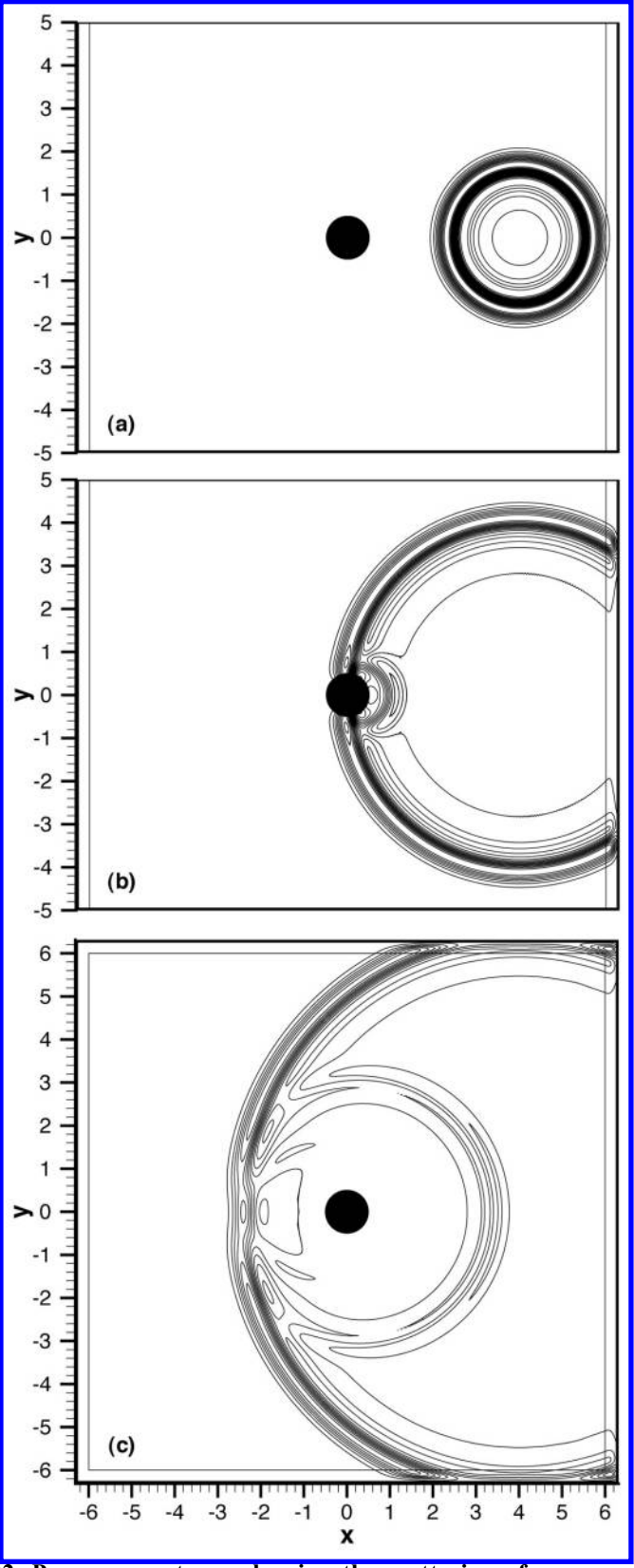


Figure 22. Pressure contours showing the scattering of an acoustic wave pulse by a circular cylinder. (a) t = 1.6. (b) t = 4.0. (c) t = 6.4. Dashed lines are the exact solution.

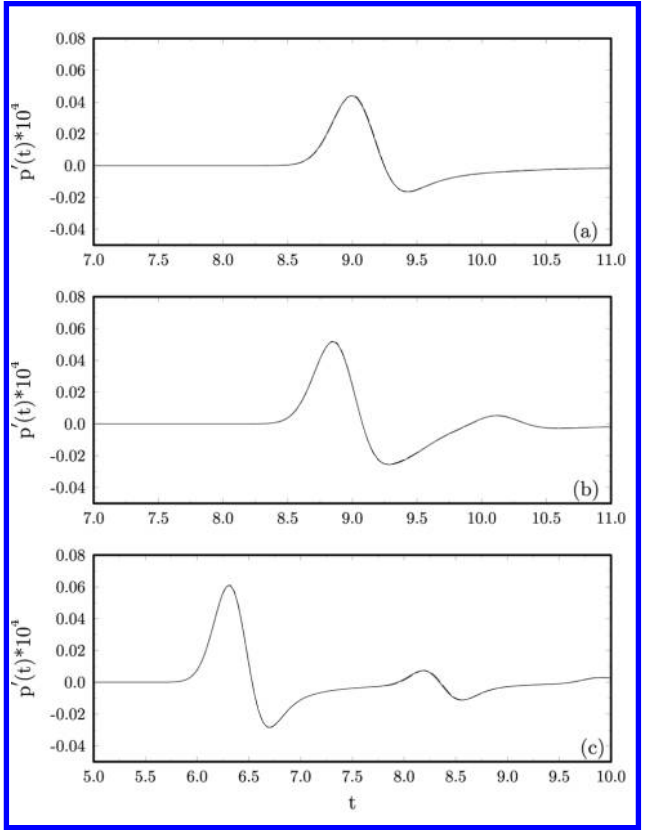


Figure 23. Time history of pressure perturbation p = p 1/p at (a) x = -5, y = 0, (b) x = -4, y = -4, (c) x = 0, y = 5. Dashed line is the exact solution.

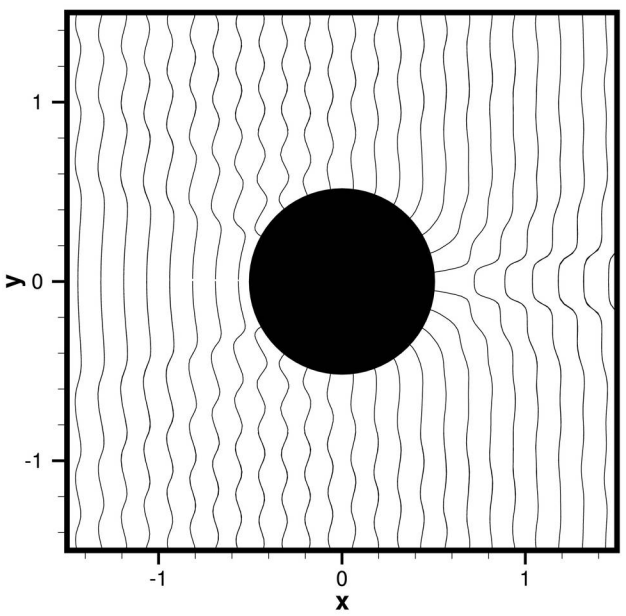


Figure 24. Zero pressure contours at the beginning of a cycle. Pressure pattern formed by the scattering of a plane wave by a cylinder. Wave length equal to quarter diameter of cylinder.

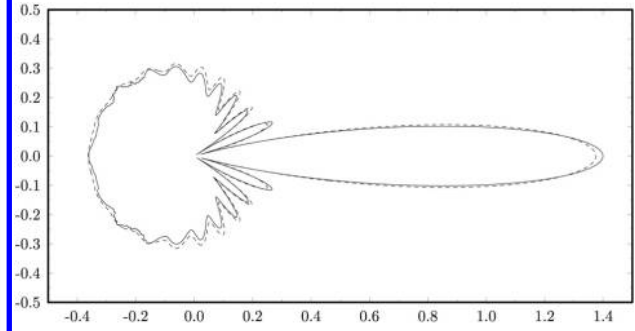


Figure 25. Comparison between computed and exact scattering cross-section. Dashed curve is the exact solution.

#### 2. Plane Wave Scattering Problem

Kurbatskii and Tam [18] solved the problem of plane wave scattering by a cylinder to illustrate the good accuracy obtained by their Cartesian boundary treatment method. Here we solve the same problem using overset grid method. One advantage of the overset grid method in this case is that the simple ghost point method [15] may be used to enforce the wall boundary condition. Again, the 7-point stencil DRP scheme is used to solve the Euler equations. The amplitude of the incoming waves with wave front perpendicular to the x-axis and wave length equal to  $8 \Box x$  is set to be small. The problem is, therefore, essentially linear and the the accuracy of the computed solution can be ascertained by comparing with exact linear solution.

Figure 24 shows the computed zero pressure contours at the beginning of a cycle. Plotted in this figure also are the contours of the exact solution in dashed line. The difference between the computed and the exact solution is very small; less than the thickness of the lines. Figure 25 shows the computed and the exact scattering cross-section  $\Box(\Box)$ , defined by

$$\Box(\Box) = \lim_{r\Box} \left( r \overline{p_s^2} \right)^{\frac{1}{2}} \tag{50}$$

where the overbar denotes time average.  $p_s$  is the pressure of the scattered acoustic waves. There is good agreement between the two. A major part of the small discrepancies arises because the computed result is measured at a finite distance from the center of the cylinder whereas the exact solution is determined by taking the limit  $r \mid \cdot|$ 

#### **B. Sliding Interface Problem**

Aircraft engine noise is a significant environmental and certification issue. Noise generated by the fan rotor wake impinging on the stator is an important noise component at both take-off and landing. In the Second CAA Workshop on Benchmark Problems, a simplified model of this noise mechanism was proposed as a benchmark problem. One important feature of the problem is a sliding interface (see Fig. 1) imitating the relative motion between a fan blade fixed computation domain and a stator blade fixed computation domain. Here a more demanding sliding interface problem is considered. It will be shown that the use of optimized interpolation scheme yields highly accurate numerical results.

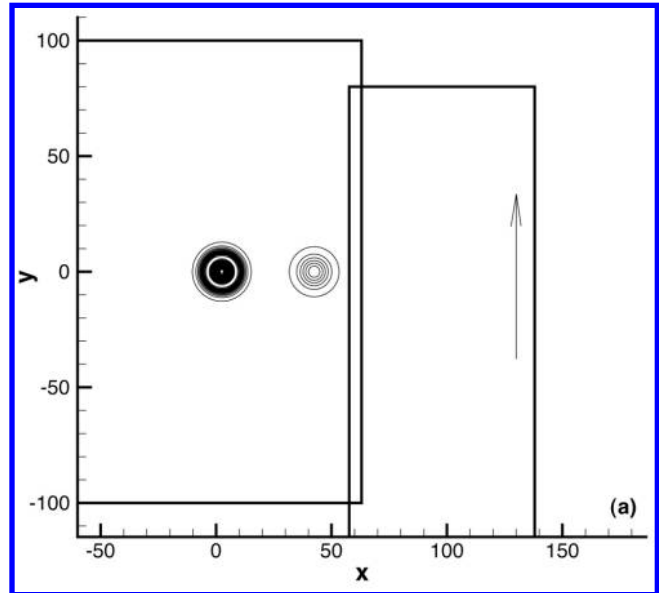


Figure 26a. Density contours showing the transmission of an acoustic and an entropy pulse across a sliding interface. Dashed lines are the exact solution. (a) t = 5.6. (b) t = 44.9. (c) t = 73.0.

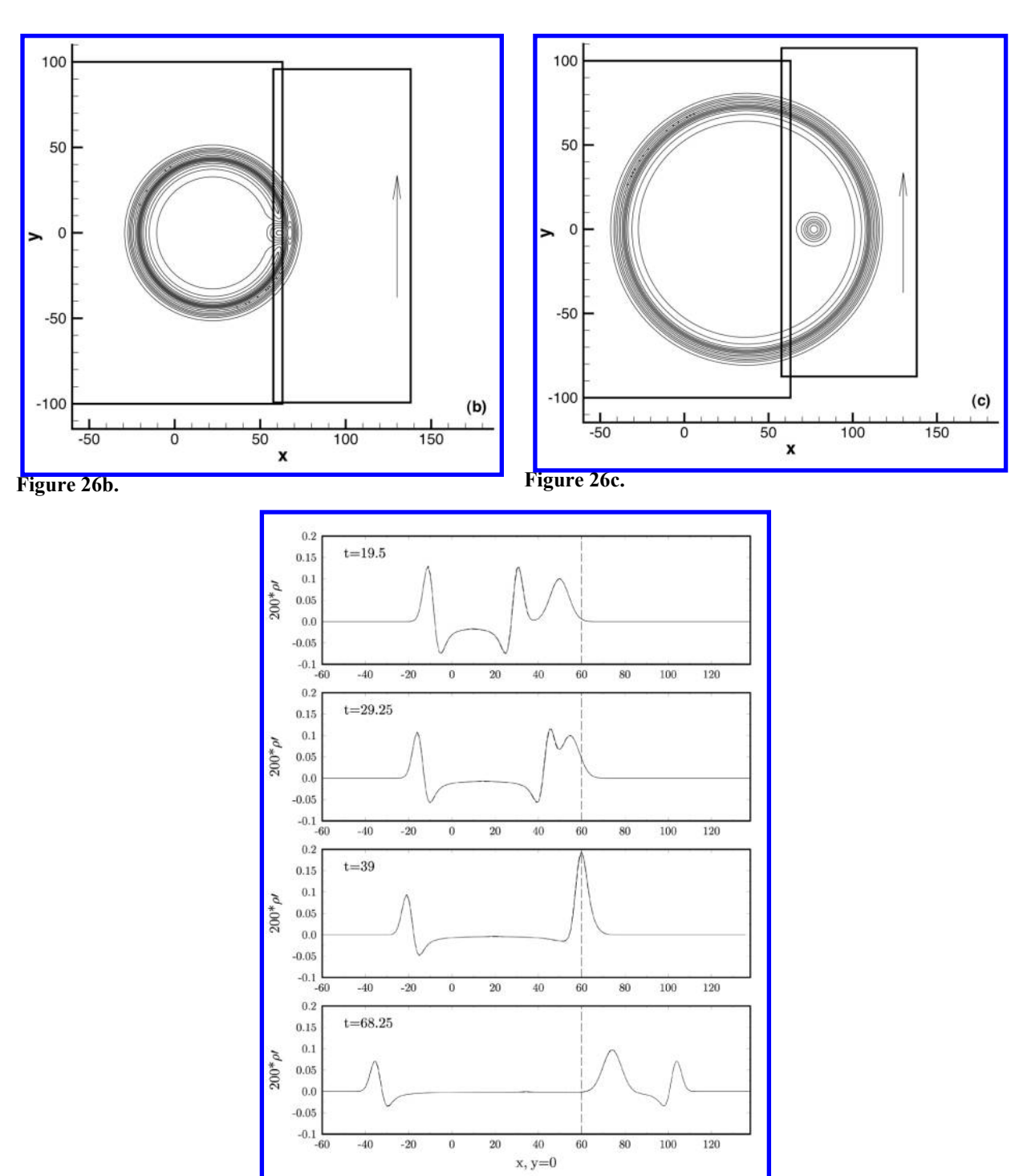


Figure 27. Spatial distribution of density perturbation  $\square \models \square \square 1$  associated with an acoustic and an entropy pulse propagating across a sliding interface located at x = 60. Dashed line is the exact solution.

Figure 26 shows two computation plane with six columns of overlapping meshes. The left computation plane is stationary. The right computation plane moves upward at a velocity of  $v_g$ . The sliding interface is the line at the center of the overlapping meshes. We will use  $(x_1, y_1)$  to denote the coordinates of a point in the stationary computation plane on the left and  $(x_2, y_2)$  the coordinates of a point in the moving computation plane on the right. The relationships between the two coordinate systems are,  $x_2 = x_1$ ,  $y_2 = y_1 \square v_g t$ . For computation purposes, we will

use  $[x_1 = y_1, x_2 = y_2 = 0.78]x_1$ . Dimensionless variables with  $[x_1]$  as length scale,  $a_0$  (the speed of sound) as the velocity scale,  $[x_1/a_0]$  as the time scale,  $[x_1/a_0]$  (mean flow density) as the density scale and  $[x_1/a_0]$  as the pressure scale are used. We will assume that there is a uniform mean flow at 0.5 Mach number in the x-direction over the entire computation domain. The x-direction is the horizontal direction in Fig. 26. The sliding interface is at x = 60.

The governing equations are the Euler equations. In the stationary computation plane, they are given by (47) with x replaced by  $x_1$  and y by  $y_1$ . In the moving computation plane, the governing equations, with respect to a grid fixed frame of reference, are:

$$\frac{\partial \square}{\partial t} + u \frac{\partial \square}{\partial x_{2}} + \left(v \square v_{g}\right) \frac{\partial \square}{\partial y_{2}} + \left(v \square v_{g}\right) \frac{\partial \square}{\partial x_{2}} + \frac{\partial v}{\partial y_{2}} = 0$$

$$\frac{\partial u}{\partial t} + u \frac{\partial u}{\partial x_{2}} + \left(v \square v_{g}\right) \frac{\partial u}{\partial y_{2}} + \frac{1}{\square} \frac{\partial p}{\partial x_{2}} = 0$$

$$\frac{\partial v}{\partial t} + u \frac{\partial p}{\partial x_{2}} + \left(v \square v_{g}\right) \frac{\partial p}{\partial y_{2}} + \frac{1}{\square} \frac{\partial p}{\partial y_{2}} = 0$$

$$\frac{\partial p}{\partial t} + u \frac{\partial p}{\partial x_{2}} + \left(v \square v_{g}\right) \frac{\partial p}{\partial y_{2}} = 0$$
(51)

At time equal to zero, a pressure pulse centered at  $x_1 = y_1 = 0$  is released. At the same time, a vorticity pulse and an entropy pulse centered at  $x_1 = 40$ ,  $y_1 = 0$  are released. Mathematically, the initial conditions at t = 0 are,

$$p = \frac{1}{\Box} + \Box \exp \left[ (\ln 2) \right] \frac{x_1^2 + y_1^2}{9}$$

$$p = 1 + \Box \exp \left[ (\ln 2) \right] \frac{x_1^2 + y_1^2}{9}$$

$$= 0.5 + 0.04 \Box y_1 \exp \left[ (\ln 2) \right] \frac{(x_1 \Box 40)^2 + y_1^2}{25}$$

$$v = \Box 0.04 \Box (x_1 \Box 40) \exp \left[ (\ln 2) \right] \frac{(x_1 \Box 40)^2 + y_1^2}{25}$$

$$= 0.04 \Box (x_1 \Box 40) \exp \left[ (\ln 2) \right] \frac{(x_1 \Box 40)^2 + y_1^2}{25}$$

$$= 0.04 \Box (x_1 \Box 40) \exp \left[ (\ln 2) \right] \frac{(x_1 \Box 40)^2 + y_1^2}{25}$$

$$= 0.04 \Box (x_1 \Box 40) \exp \left[ (\ln 2) \right] \frac{(x_1 \Box 40)^2 + y_1^2}{25}$$

$$= 0.04 \Box (x_1 \Box 40) \exp \left[ (\ln 2) \right] \frac{(x_1 \Box 40)^2 + y_1^2}{25}$$

where  $\Gamma = 0.005$  and  $\Gamma = 1.4$ . In the course of time, the acoustic, the vorticity and the entropy pulse will all be propagating or convected downstream. They will all reach the sliding interface at nearly the same time. They will then move across the sliding interface into the moving grid farther downstream.

In the computation, the 7-point stencil DRP scheme is again used. For points on the stationary grid, the unknowns on every grid point including those on the sliding interface are determined at every time step by solving equation (47). Similarly, for points on the moving grid, the unknowns on every grid point including those on the sliding interface are updated according to (51). The unknowns of the three extra columns of grid points extending beyond the sliding interface cannot be calculated by the 7-point stencil DRP scheme. They are found by optimized interpolation using a 16-point stencil from the values of the variables on the other grid. In this way, information of the solution is passed between the two computation grids.

Figures 26a, 26b and 26c show the computed density contours associated with the acoustic and entropy pulses at time t = 5.6, 44.9 and 73.0. In this computation  $v_g$  is set equal to 0.4. Also plotted in these figures are contours of the exact solution in dashed lines (see Category 3, Problem 1 of Ref. [19]). Because the difference between the computed and the exact solution is small the dashed lines may not be easily detected. In Fig. 26a, the two pulses are in the stationary grid. Figure 26b shows that the acoustic pulse moving downstream at three times the velocity of the entropy pulse catches up with the entropy pulse right at the sliding interface. Figure 26c shows that the entropy pulse

has now been convected past the sliding interface onto the moving grid. At this time, the acoustic pulse has already propagated further downstream. Figure 27 shows the computed and the exact density waveform along the x-axis at four different times. The sliding interface is located at x = 60. It is clear from these figures that the treatment of a sliding interface using optimized interpolation is extremely effective and accurate.

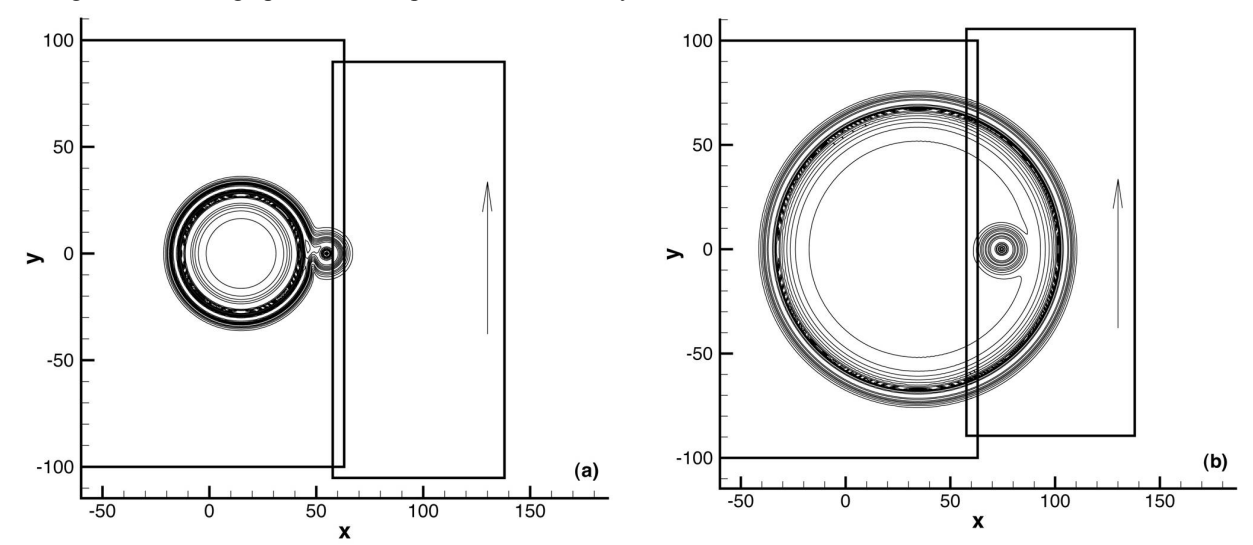


Figure 28a. Contours of fluid velocity  $(u[]+v[])^{1/2}$  associated with the transmission of an acoustic and a vorticity pulse across a sliding interface. Dashed lines are the exact solution. (a) t = 28.1. (b) t = 67.3.



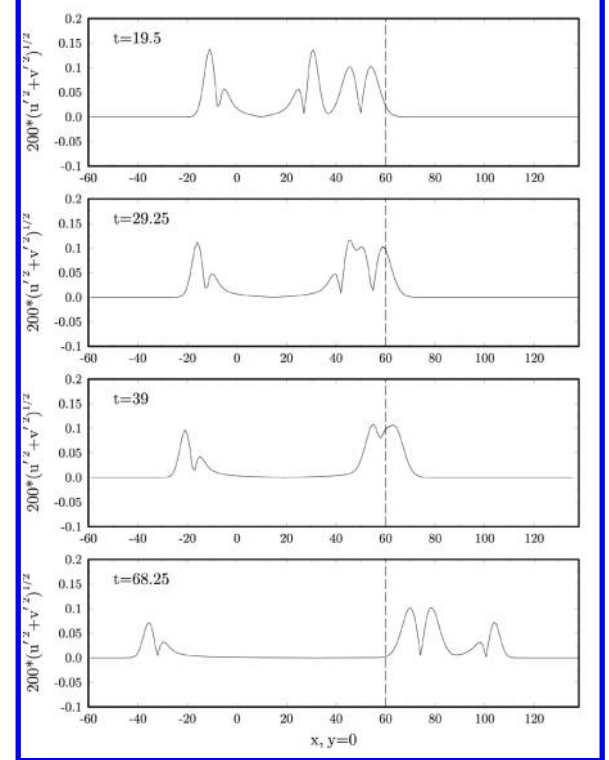


Figure 29. Spatial distributions of fluid velocity perturbation  $(u + v)^{1/2}$ , where u + u = 0.5, v + v, associated with the transmission of an acoustic and a vorticity pulse across a sliding interface at x = 60. Dashed line is the exact solution.

Figures 28a and 28b show the computed and the exact fluid velocity,  $(u[]+v[])^{1/2}$ , contours of the acoustic and vorticity pulses as they propagate through the sliding interface. Again, the difference between the computed and exact contours, being less than the thickness of the contour lines, is difficult to detect. Figure 29 shows the waveform along the x-axis at four instances of time. At t = 29.25 to t = 39 the two pulses merge and propagate across the sliding interface together. At time t = 68.25, the acoustic pulse has passed through the entropy pulse and the two pulses are now separated. The computed waveforms are in excellent agreement with exact solution.

We would like to add that we have recomputed the above problem by setting  $v_g$  to a supersonic speed at Mach 1.1. We found that the numerical results are identical to the computation at  $v_g = 0.4$ . This suggests that the present method is capable of treating the sliding interface of rotor-stator interaction problem at supersonic blade tip speed.

# VI. Summary

In this paper, a method that quantifies interpolation error in multi-dimensions using either a regular or irregular stencil is developed. Based on this method, a multi-dimensional optimized interpolation scheme is proposed. This scheme minimizes the interpolation error in wave number space. The scheme allows the imposition of order constraints. Order constraints require the interpolation to satisfy Taylor series expansion with respect to grid point spacing to a specified order. It is shown that the effect of order constraints is to reduce interpolation error over the low wave number region in wave number space. On the other hand, there is an increase in error for high wave numbers.

An interpolation stencil may be regular with respect to one curvilinear coordinate system but when another curvilinear coordinate system is used as the frame of reference, the stencil is irregular. In this work, an example is provided to demonstrate that for global interpolation, the use of regular stencils leads to a lower level of error. For this reason, it is the preferred choice. Comparisons between the errors of the proposed optimized interpolation method and those of the standard methods are provided. It is shown that large interpolation error would incur if tensor products are used as basis functions for interpolation. It is also demonstrated that the use of ordered polynomial basis functions has error map that resembles that of the optimized interpolation method under maximum order constraint.

Currently, a number of large stencil, high resolution methods are available in the literature for solving CAA problems with good accuracy. However, they are designed for use only on structured grids. To treat acoustic problems with complex geometry, the overset grid method may be adopted. To implement this approach, one may use one of the high resolution CAA algorithm as the basic computation scheme and the optimized interpolation scheme for the data transfer between grids. This will ensure a uniformly high resolution numerical solution in the entire computation domain. In this paper, examples are provided to illustrate this computation strategy and to show that highly accurate computed solution can be obtained. It is also demonstrated that this method is useful to treat problems involving sliding interface. Although not discussed, the same method with slight modifications may be used to solve problems with well defined moving boundaries.

# Appendix A: Computation of the Values of the Elements of Matrix A as $x_j \square x_k$

As alluded to before, when the stencil points are aligned on a coordinate line, the limit form of the matrix elements as given by (15) and (19) are to be used; e.g.,

$$\lim_{x_{j} \square x_{k}} \frac{\square \sin(\square(x_{j} \square x_{k})/\square)}{(x_{j} \square x_{k})} = \square$$

However, for points very nearly aligned, direct numerical evaluation of the matrix or vector elements is not recommended because of the division by a small number. Instead, we advise that the limit values be used whenever  $|x_j \square x_k| < \overline{\square}$ . To find a suitable value of |I|, let us consider the error incurred when  $(\square/(x_j \square x_k))\sin(\square(x_j \square x_k)/\square)$  is approximated by its limit value |I| where  $|x_j \square x_k| < \overline{\square}$ . Let  $\square = (x_j \square x_k)/\square$ , we have by Taylor series expansion,

$$\sin\left(\frac{1}{2}\right) = \frac{1}{2}\left(\frac{1}{2}\right)^{3} + \frac{1}{2}\left(\frac{1}{2}\right)^{5} + \frac{1}$$

It is easy to establish

$$\left|\sin\left(\square\square\right)\square\square\square\right| \square \frac{\left(\square\square\right)^3}{3!}$$

or

$$\frac{\left|\frac{\sin(\square)}{\square}\square\square}{\square}\square\square\right| \square \frac{\left(\square\square\right)^2}{3!}$$

Thus the relative error of using the limit value to approximate the relevant parts of a matrix element is less than  $( \square^2 / 3!) ( \square / \square )^2$ . We recommend to take  $\square / \square = 10^{\square 5}$  for  $\square = 1.2$ . In this case, the relative error is less than  $2.4 \square 10^{\square 11}$ . This is an extremely small error.

# Appendix B: Coordinates of the 16-Point Irregular Stencil of Figure 2

| appendia D.                       | Coordinates of the 10 1 offic fri |
|-----------------------------------|-----------------------------------|
| The coordinates $(x_j, y_j)$ are: | (-0.70, 1.72)                     |
|                                   | (0.34, 1.58)                      |
|                                   | (1.24, 1.14)                      |
|                                   | (-1.62, 0.72)                     |
|                                   | (-0.38, 0.79)                     |
|                                   | (0.64, 0.60)                      |
|                                   | (-1.02, 0.08)                     |
|                                   | (0.18, -0.20)                     |
|                                   | (1.58, 0.06)                      |
|                                   | (-1.24, -0.56)                    |
|                                   | (-0.38, -0.92)                    |
|                                   | (0.800.78)                        |
|                                   | (-1.56, -1.40)                    |
|                                   | (-0.26, -1.68)                    |
|                                   | (0.66, -1.52)                     |
|                                   | (1.64, -1.16)                     |
| The points to be interpolated a   | e: A (-0.40, 0.30)                |
|                                   | B(0.00, 0.00)                     |
|                                   | C (-0.40, 0.00)                   |
|                                   | D(1.00, 0.00)                     |

# Appendix C: Derivation of an Exact Solution for the Scattering of an Acoustic Pulse by a Circular Cylinder

In this appendix, we derive an exact solution for the scattering of an acoustic pulse by a circular cylinder. The solution provided in Ref. [17] is incorrect. Let the cylinder be centered at (x, y) = (0, 0) with a radius  $r_0$  and the acoustic pulse be initialized as

$$p(x, y, 0) = e^{\Box b[(x \Box x_s)^2 + (y \Box y_s)^2]}, \quad u = v = 0 \text{ at } t = 0$$
 (C1)

where p is the pressure, (u, v) is the velocity, and  $b = (\ln 2)/d^2$  in which d is the pulse half-width. As in Ref. [17], the solution will be found in terms of the velocity potential  $\square$  defined as

$$p = \Box \frac{\partial \Box}{\partial t}, \qquad u = \frac{\partial \Box}{\partial x}, \qquad v = \frac{\partial \Box}{\partial v}$$
 (C2)

Let

$$\Box(x,y,t) = \Box_i(x,y,t) + \Box_r(x,y,t)$$

where  $\prod_i(x, y, t)$  represents the wave generated by the pulse in the free space and  $\prod_r(x, y, t)$  represents the wave reflected by the cylinder. The solution for  $\prod_i(x, y, t)$  has been found in Ref. [16],

$$\Box_{i}(x,y,t) = \operatorname{Im} \Box_{0} A_{i}(x,y,\Box) e^{\Box i\Box t} d\Box \Box$$
(C3)

where

$$A_i(x, y, \square) = \frac{1}{2h} e^{\square \square^2/(4h)} J_0(\square r_s)$$
 (C4)

and  $r_s = \sqrt{(x \square x_s)^2 + (y \square y_s)^2}$ . Here Im{} and Re{} denote the imaginary and real part of {}, respectively, and  $J_k$  denotes the Bessel function of order k.

To find  $\square_r$ , following (C3), we assume

$$\Box_r(x,y,t) = \operatorname{Im} \Box_0 A_r(x,y,\Box) e^{\Box i\Box t} d\Box \Box$$
(C5)

in which  $A_r(x, y, \square)$  satisfies the Helmholtz equation

$$\frac{\Box \partial^2 A_r}{\partial x^2} + \frac{\partial^2 A_r}{\partial y^2} \Box + \Box^2 A_r = 0$$

and the following solid wall boundary condition on the cylinder,

$$\frac{\partial A_r}{\partial r} = \prod_{i=0}^{\infty} \frac{\partial A_i}{\partial r} \quad \text{at} \quad r = r_0$$
 (C6)

 $A_r$  can be solved by a method of separation of variables in the polar coordinates  $(r, \square)$  that gives the following expansion

$$A_r(x, y, \square) = \prod_{k=0} C_k(\square) H_k^{(1)}(r\square) \cos(k\square)$$
(C7)

In (C7),  $H_k^{(1)}$  is the Hankel function of the first kind of order k. The expansion in (C7) ensures that  $\square_r$  will satisfy the far field radiation condition. Then the boundary condition (C6) leads to

$$\prod_{k=0} C_k \left( \square \right) \square H_k^{(1)} \square \left( r_0 \square \right) \cos \left( k \square \right) = \frac{1}{2b} e^{\square \square^2 / (4b)} \square J_1 \left( \square r_{s_0} \right) \frac{r_0 \square x_s \cos \square \square y_s \sin \square}{r_{s_0}} \tag{C8}$$

where

$$r_{s_0} = r_s \mid_{r=r_0} = \sqrt{r_0^2 \, \Box \, 2r_0 x_s \cos \Box \Box \, 2r_0 y_s \sin \Box + x_s^2 + y_s^2}$$

On considering the left side of (C8) as a Fourier cosine series in  $\Pi$ , it is straightforward to find,

$$C_{k}(\square) = \frac{\square}{2b} e^{\square \square^{2}/(4b)} \frac{\square}{\square \square H_{k}^{(1)\square}(r_{0}\square)} \frac{\square}{0} J_{1}(\square r_{s_{0}}) \frac{r_{0}\square x_{s} \cos \square\square y_{s} \sin \square}{r_{s_{0}}} \cos(k\square) d\square$$

where  $\square_k = 1$  and  $\square_k = 2$  for  $k \neq 0$ .

Finally, the total pressure field can be found as follows,

$$p(x,y,t) = \Box \frac{\partial \Box}{\partial t} = \frac{\partial}{\partial t} (\Box_i + \Box_r)$$

$$= \operatorname{Re} \Box \Box (A_i(x,y,\Box) + A_r(x,y,\Box)) \Box \Box^{ij\Box t} d\Box \Box$$

where  $A_i(x, y, \square)$  is given by (C4) and  $A_r(x, y, \square)$  by (C7).

## Acknowledgment

This work was supported by the Aeroacoustics Research Consortium through a subcontract from the Ohio Aerospace Institute.

#### References

- <sup>1</sup> C.K.W. Tam, Computational Aeroacoustics: issues and methods, AIAA J. 23 (1995) 1788--1796.
- <sup>2</sup> C.K.W. Tam, Computational Aeroacoustics: an overview of computational challenges and applications, International J. Comput. Fluid Dynamics (to appear 2004).
- J.F. Groneneg, "Turbomachinery noise" in Aeroacoustics of Flight Vehicles: Theory and Practice, vol. 1. ed. H.H. Hubbard, NASA RP-1258, pp. 1788--1796 (1995).
- <sup>4</sup> E. Envia, A.G. Wilson, D.L. Huff, Fan noise: a challenge to CAA, International J. Comput. Fluid Dynamics (Special Issue on CAA; to appear 2004).
- B. Singer, Y. Guo. Development of CAA tools for airframe noise calculations, International J. Comput. Fluid Dynamics (Special Issue on CAA; to appear 2004).
- <sup>6</sup> J.W. Delfs, An overlapped grid technique for high resolution CAA schemes for complex geometries, AIAA Paper 2001-2199 (2001).
- J. Yin, J.W. Delfs, Sound generation from gust-airfoil interaction using CAA-chimera method, AIAA Paper 2001-2136
  - <sup>8</sup> Y. Lee, J.D. Baeder, High-order overset method for blade vortex interaction, AIAA Paper 2002-0559 (2002).
- <sup>9</sup> S.E. Scherer, J.N. Scott, Development and validation of a high-order overset grid flow solver, AIAA Paper 2002-2733
- <sup>10</sup>S.E. Scherer, M.R. Visbal, Computational study of acoustic scattering from multiple bodies using a high-order overset grid approach, AIAA Paper 2003-3203 (2003).
  - S.K. Lele, Compact finite difference schemes with spectral-like resolution, J. Comput. Phys. 103 (1992) 16--42.
- <sup>12</sup> C.K.W. Tam, K.A. Kurbatskii, A wavenumber based extrapolation and interpolation method for use in conjunction with high-order finite difference schemes, J. Comput. Phys. 157 (2000) 588-617.
  - S.E. Scherer, J.N. Scott, Comparison of highly accurate interpolation methods, AIAA Paper 2001-0282 (2001).
- <sup>14</sup> C.K.W. Tam, J.C. Webb, Z. Dong, A study of the short wave components in computational acoustics, J. Comput. Acoustics 1 (1993) 1--3.
- <sup>15</sup> C.K.W. Tam, Z. Dong, Wall boundary conditions for high-order finite difference schemes in computational aeroacoustics, Theoretical and Computational Fluid Dynamics 6 (1994) 303--322.
- <sup>16</sup> C.K.W. Tam, J.C. Webb, Dispersion-Relation-Preserving finite difference scheme for computational acoustics, J. Comput. Phys. 107 (1993) 262--281.
- C.K.W. Tam, J.C. Hardin ed. Proceedings of the Second Computational Aeroacoustics Workshop on Benchmark Problems, NASA CP 3352 (1997).
- <sup>18</sup> K.A. Kurbatskii, C.K.W. Tam, Cartesian boundary treatment of curved walls for high-order computational aeroacoustics schemes, AIAA J. 35 (1997) 133--140.
- J.C. Hardin, J.R. Ristorcelli, C.K.W. Tam, Proceedings of ICASE/LaRC Workshop on Benchmark Problems in Computational Aeroacoustics, NASA CP 3300 (1995).

## This article has been cited by:

- 1. Yuma Fukushima, Takashi Misaka, Shigeru Obayashi, Daisuke Sasaki, Kazuhiro Nakahashi. Wavenumber Optimized Immersed Boundary Method for Aeroacoustic Analysis Based on Cartesian Mesh. *AIAA Journal*, ahead of print0-0. [Abstract] [Full Text] [PDF] [PDF Plus]
- 2. Ahmed A. Hemeda, Basman Elhadidi. 2014. Domain Decomposition Technique for Solution of Acoustic Wave Scattering. *AIAA Journal* 52:2, 408-418. [Abstract] [Full Text] [PDF] [PDF Plus]
- 3. X. X. Chen, X. Zhang. 2013. High-Order Interface for Aeroacoustic Computation Using Overset Grid. *AIAA Journal* 51:2, 519-523. [Citation] [Full Text] [PDF] [PDF Plus]
- 4. Georg Geiser, Seong Ryong Koh, Wolfgang SchröderAnalysis of acoustic source terms of a coaxial helium/air jet . [Citation] [PDF] [PDF Plus]